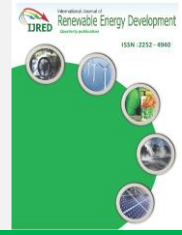




Contents list available at IJRED website

**International Journal of Renewable Energy Development**

Journal homepage: <https://ijred.undip.ac.id>



Research Article

# Enhancing transient stability and dynamic response of wind-penetrated power systems through PSS and STATCOM cooperation

Khaled Kouider\* and Abdelkader Bekri

*The Control, Analysis and Optimization of the Electro-Energetic Systems (CAOSEE) Laboratory, Tahri Mohamed University, Bechar, Algeria*

**Abstract.** The large-scale integration of doubly-fed induction generator (DFIG) based wind power plants poses stability challenges for power system operation. This study investigates the transient stability and dynamic performance of a modified 3-machine, 9-bus Western System Coordinating Council (WSCC) system. The investigation was conducted by connecting the DFIG wind farm to the sixth bus via a low-impedance transmission line and installing power system stabilizers (PSSs) on all automatic voltage regulators (AVRs). A three-phase fault simulation was carried out to test the system, with and without power system stabilizers and a static synchronous compensator (STATCOM) device. Time-domain simulations demonstrate improved transient response with PSS-STATCOM control. A 50% reduction in settling time and 70% decrease in power angle undershoots at the slack bus are achieved following disturbances, even at minimum wind penetration levels. Load flow analysis shows the coordinated controllers maintain voltages within 0.5% of nominal at 60% wind penetration, while voltages at load buses can deviate up to 15% without control. Eigenvalue analysis indicates the PSS-STATCOM boosts damping ratios of critical oscillatory modes from nearly 0% to over 30% under high wind injection. Together, the present findings provide significant evidence that PSS and STATCOM cooperation enhances dynamic voltage regulation, angle stability, and damping across operating ranges, thereby maintaining secure operation in systems with high renewable integration.

**Keywords:** Doubly-Fed Induction Generator, Power System Stabilizer, Transient Stability, Power System Oscillations, Static Synchronous Compensator, Western System Coordinating Council



@ The author(s). Published by CBIORE. This is an open access article under the CC BY-SA license (<http://creativecommons.org/licenses/by-sa/4.0/>).

Received: 15<sup>th</sup> March 2023; Revised: 10<sup>th</sup> June 2023; Accepted: 18<sup>th</sup> July 2023; Available online: 25<sup>th</sup> July 2023

## 1. Introduction

Renewable energy has become a new area of study due to growing concerns about climate change and the limitation of fossil fuels. Renewable energy sources such as wind and solar can help reduce the reliance on traditional fossil fuels. Wind turbines' reliability and durability increase with the wind farm penetration level. Wind farms must supply the appropriate amount of electricity based on the grid's wind speed and energy demand (Simani & Farsoni, 2018). DFIG wind technologies are becoming increasingly popular in the renewable energy sector due to their high level of efficiency in relation to their cost (Miller, 2010; Yunus *et al.*, 2019).

With the broad penetration of these intermittent energy sources, power system stability can be affected in the case of insufficient control and poor damping. Conceptually and from a heuristic standpoint, a system is considered stable if it can maintain equilibrium under normal conditions and return to an acceptable equilibrium after being disturbed (Prabha, 1994). Loss of synchronism between rotating inertias, low voltages, natural disturbances, or protection system malfunctions can all potentially cause power system instability (Eremia & Shahidehpour, 2013).

Power system stability can be categorized into three main types: rotor angle, voltage, and frequency stability. In (Asija *et al.*, 2015), MATLAB was used to perform contingency analysis and power flow studies on a WSCC 9-bus test system to

investigate its stability and dynamics. Recently, the impact of DFIG wind turbines on power system stability has gained considerable attention due to advances in wind power conversion technology. Integrating DFIG wind turbines into power systems raises particular concerns regarding small-signal stability, which involves the ability to recover and maintain equilibrium after minor disturbances.

Nkosi *et al.*, (2023) analyze small signal stability in power systems with Doubly Fed Induction Generators. They review the latest advancements in modeling DFIG-based wind farms and examine control techniques that improve the damping properties of the power system. Squirrel cage induction generator (SCIG) and DFIG implementations in a 14-bus IEEE system investigate small signal stability in (Chandra *et al.*, 2014), and simulation results are reported. As stated in (Bagchi *et al.*, 2016), analogous functions of Static VAR compensator (SVC) and STATCOM are embedded in DFIGs for small signal stability requirements. In (Pérez-Londoño *et al.*, 2012), the impact of DFIGs on power system voltage stability was studied, and deduce that only small-scale wind power penetration preserves stability.

Large power systems face numerous challenges related to transient stability. A stable state after a disturbance is called post-fault equilibrium, and it indicates the ability of the system to return to a pre-fault state following significant disturbances, such as faults, overloads, or generator unit failures

\* Corresponding author  
Email: [khouiledkhaled@gmail.com](mailto:khouiledkhaled@gmail.com) (K. Kouider)

(Hatzargyriou *et al.*, 2021; Ramanujam, 2010; Xu *et al.*, 2023). There has been extensive research aimed at assessing transient stability in wind power systems. (Reza *et al.*, 2003) examines how the transient stability of the transmission system is affected by distributed generation (DG) and analyzes various DG technologies and their levels of penetration in the power system. In (Morshed, 2020), a coordination strategy using the zero-dynamics technique to ameliorate the transient stability of IEEE 39-bus power systems, including doubly-fed induction generators (DFIGs), under varying operating conditions. (Xia *et al.*, 2018) analyzes the impact of wind power generation on power system transient stability during changes in energy flow. Specifically examining the effects of wind farms' location, speed, and capacity on the stability of the IEEE 14-bus system. The study (Pillai *et al.*, 2013) examines the transient stability of wind power systems with storage utilizing a central zone controller. (Edrah *et al.*, 2015) analyze insightfully the impact of controlling and operating the DFIG on the rotor angle stability of power systems. They propose addressing this issue by implementing a PSS on the reactive control loop for the rotor-side converter (RSC) and reconfiguring the grid-side converter (GSC) to function as a STATCOM, which aims to minimize the influence of the DFIG on the overall stability of the power system.

The transient stability of wind farms in multi-machine power systems can be enhanced using fuzzy controllers based on STATCOMs and SVCs, as demonstrated in (M. Hemeida, H. Rezk, and M. Hamada, 2018). Meanwhile, simulation results in (Fdaili *et al.*, 2021) show that the proposed uncontrolled fault current limiter (NCFCL) with reactive power back-up is a better approach than crowbar protection for enhancing Fault Ride Through (FRT) capabilities. A method for stabilizing rotor angle is proposed in (Zheng *et al.*, 2019), which is based on the phase-amplitude characteristics of grid transient voltage. The impact of DFIGs on the system is assessed using an index that reflects variations in the acceleration area of synchronous generators. The simulation outcomes confirm that the strategy works well. (Cai, Dong, & Liao, 2021) examines the dynamic performance of wind turbines under extreme grid disturbances, particularly through zero-voltage ride-through (ZVRT). During ZVRT, the reactive response of a doubly-fed (type-3) wind turbine is influenced by the converter's control technique and the steady-state and transient-state performance of the DFIG.

Reference (Alsakati *et al.*, 2022) studies adjusting the transient stability of a two-zone, four-machine wind energy system using the multiple-band power system stabilizer (OMB-PSS4C). (Eshkaftaki *et al.*, 2020) propose two methods to improve the transient and dynamic stability of the local synchronous generator (SG). The first method is a genetically tuned electromagnetic torque band damping controller (ETBDC), and the second method is a reactive power band damping controller (RPBDC) utilizing the suggested transient controller (TC) for transient stability. Under temporary disturbances, the TC transitions the DFIG operation from generator to motor speed, while the ETBDC and RPBDC significantly improve the dynamic performance of the SG.

The study (Agarala *et al.*, 2022) presents a new control technique called automatic reactive power support (ARS) that enhances multi-machine power system stability by injecting available reactive power during faults through converters. The comparative analysis across different test cases, including scenarios with different types of renewable sources, such as wind generators like permanent magnet synchronous generators (PMSG) and doubly fed induction generators, as well as solar PV, demonstrates the effectiveness of the proposed control technique in improving system stability and critical

clearing time. The impacts of a closed-loop DFIG model on the transient stability of a power system with high penetration of DFIG wind energy are thoroughly examined (Shabani, Kalantar, & Hajizadeh, 2021a). An innovative method for real-time transient instability (TID) detection is described in (Shabani & Kalantar, 2021b). Utilizing a transient energy function, this approach is deployed in a power system with a high penetration of DFIG wind farms. TID in a shorter time is achieved using the proposed strategy, according to simulation findings.

The issue of power system oscillations poses significant concerns in the field of power system stability. Several factors may contribute to these oscillations, including torque imbalances, insufficient damping, inadequate controller tuning, and including interactions between controllers and transmission lines compensated by series capacitors (Eremia & Shahidehpour, 2013; Prabha, 1994;). Moreover, the frequency ranges (0.1-0.8 Hz) and (1-2 Hz) enable the identification of two distinct oscillation modes in the power system, namely local and inter-area modes. These Electro-Mechanical oscillation modes were investigated in previous works as cited in references (Avdakovic *et al.*, 2009; Klein, Rogers, & Prabha, 1991; Yang *et al.*, 2011). Other studies analyzed and compared various aspects of power system stability, including oscillation damping (Edrah *et al.*, 2016; Falehi *et al.*, 2012; Li *et al.*, 2022; Thanpisit & Ngamroo, 2017; Zhang *et al.*, 2018). The findings of (Edrah *et al.*, 2016) indicate that incorporating conventional fixed parameter PSS into the reactive power control loop of the DFIG rotor-side converter has a favorable damping effect across various operating conditions. In addition, the study demonstrates that DFIG-based wind farms equipped with the suggested farm-level PSS exhibit superior effectiveness in attenuating power system oscillations compared to PSS used in Synchronous Generators. Moreover, it is possible to enhance power system stability by optimizing and coordinating additional controllers based on SVCs and PSSs, using a genetic algorithm (GA) as proposed by (Falehi *et al.*, 2012). Furthermore, the optimization model for power oscillation dampers (POD) parameters described by (Li *et al.*, 2022) incorporates the constraint of the DFIG to mitigate the oscillations of both the DFIG and the power grid. Per small-signal and transient stability measurements, the PSS and POD recommended in the study by (Thanpisit & Ngamroo, 2017) show noticeably better damping performance than traditional PSS and POD controllers in various operating conditions and fault scenarios. Per (Zhang *et al.*, 2018), inter-area modes can be effectively suppressed by employing both PSS and TCS in interconnected power systems of New England and New York, as shown by the implementation of a specific design approach.

In contrast, based on the author's review, very few publications are available in the literature that address the issue of transient stability in parallel with damping power oscillation types (Gurung & Kamalasan, 2020; He *et al.*, 2022; Morshed & Fekih, 2019; Yu *et al.*, 2018). A model-based reduced-order optimal oscillation damping controller (OODC) for a large-scale wind farm with a dual-fed induction generator was demonstrated in (Gurung & Kamalasan, 2020). Simulation results using a matched IEEE 68 bus network demonstrate that the suggested OODC effectively improves the inter-area mode damping of the system. (He *et al.*, 2022) proposes a combined approach of STATCOM, POD controller, and PSSs to enhance power system stability. An intelligent optimization algorithm, integrating GA and particle swarm algorithm (PSO), is implemented to surmount local convergence challenges. Numerical simulations on IEEE systems demonstrate the effectiveness of the method in suppressing low-frequency

power oscillation in the wind-PV-thermal-bundled (WPTB) systems. The study in (Morshed & Fekih, 2019) proposes a modified imperialist competitive algorithm (MICA) and a stochastic eigenvalue approach to combine the power system stabilizers settings of the synchronous generator, the power oscillation dampers of the DFIG, and the controllers of the static synchronous compensator to improve the dynamic stability of the power system. The proposed solution tests on a modified 39-bus New England power system under different wind conditions. The performance of the system evaluates using time-domain analysis, eigenvalue mapping, and robustness analysis. Reference (Yu et al., 2018) introduce an innovative strategy called Improved Adaptive Phasor Power Oscillation Damping (EAPPOD) to adjust for time-varying communication latencies and mitigate low-frequency oscillations in inter-area signals due to external disturbances in a complex power system with DFIG wind farm.

The current paper examines the impact of a DFIG wind farm on the transient stability and dynamic performance of a modified nine-bus WSCC power system. Despite encouraging advancements in previous studies (Gurung & Kamalasadnan, 2020; He et al., 2022; Morshed & Fekih, 2019; Yu et al., 2018), detailed investigations into voltage stability and reactive power support are still needed.

The paper begins with discussing the influence of high penetration of wind sources on power system reliability and stability, then provides a brief statement on power system stability classifications. The topic of transient stability of large power systems, including DFIG wind farms, then analyzes in depth, emphasizing the notion and nature of oscillation in power systems. The paper explains the primary purpose of power system stabilizers, which is to maintain rotor angle stability after a large disturbance and effectively handle the two types of oscillations. Further, the main objective of the STATCOM equipment is providing enough reactive power to recover the voltage profile safely under harsh operating conditions. Finally, the paper suggests a combination of PSSs/STATCOM to address both the rotor angle stability problem and provide strong reactive power support in the event of a three-phase grid fault and significant wind power penetration. The study uses the MATLAB-based Power System Analysis Toolbox (PSAT) to measure the system performance.

## 2. System Modeling

The dynamic models of synchronous machines that are suitable for stability investigations have been thoroughly discussed in (Prabha, 1994; Shabani et al 2021a). This section focuses primarily on DFIG modeling. DFIG wind turbines connect properly to the power grid through back-to-back converters, as depicted in Figure 1.

### 2.1 DFIG dynamic modeling

Details of the DFIG-based wind turbine's mathematical modelling as well as its electrical equations can be found in (Tang et al., 2018; Yang et al., 2016). As a result, utilizing the extensive set of equations in (Muñoz & Cañizares, 2011) that describe the DFIG model, certain assumptions can be made. Specifically, the stator and rotor flux dynamics are faster compared to grid dynamics. Additionally, the converter controls decouple the generator and grid interactions. Based on these assumptions, the following outcomes can be derived:

$$v_{ds} = -R_s i_{ds} + (x_s + x_m) i_{qs} + x_m i_{qr} \quad (1)$$

$$v_{qs} = -R_s i_{qs} - (x_s + x_m) i_{ds} + x_m i_{dr} \quad (2)$$

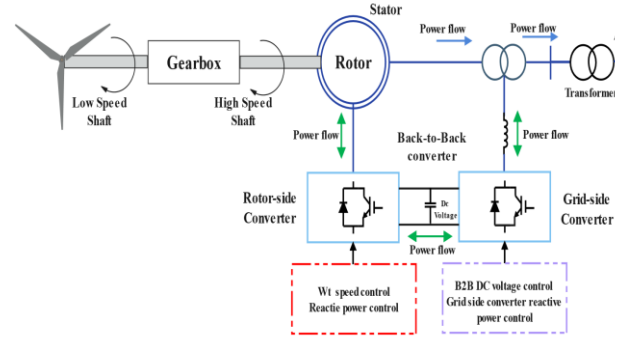


Fig. 1 A grid-connected DFIG wind system's typical configuration.

For the rotor circuit:

$$v_{dr} = -R_r i_{dr} - (1 + \omega)((x_r + x_m) i_{qr} + x_m i_{qs}) \quad (3)$$

$$v_{qr} = -R_r i_{qr} - (1 - \omega)((x_r + x_m) i_{dr} + x_m i_{ds}) \quad (4)$$

Where  $v_{ds}, v_{qs}, v_{dr}, v_{qr}$  are dq components of the stator and rotor voltages.  $i_{ds}, i_{qs}, i_{dr}, i_{qr}$  are the d and q axes stator and rotor currents.  $R_s, R_r$  are the resistances of both the stator and the rotor.  $x_s, x_r, x_m$  stator, rotor, and mutual inductances.  $\omega$  is the rotor speed.

The electromagnetic torque may therefore be expressed as:

$$T_e = x_m (i_{qr} i_{qs} - i_{ds} i_{dr}) \quad (5)$$

Additionally, the active and reactive powers for both the stator and rotor can be expressed as follows:

$$P_s = v_{ds} i_{ds} + v_{qs} i_{qs} \quad (6)$$

$$Q_s = v_{qs} i_{ds} - v_{ds} i_{qs} \quad (7)$$

$$P_r = v_{dr} i_{dr} + v_{qr} i_{qr} \quad (8)$$

$$Q_r = v_{qr} i_{dr} - v_{dr} i_{qr} \quad (9)$$

With  $P_s, Q_s$  are the active and reactive powers, while the rotor active and reactive powers are presented by  $P_r, Q_r$  in that order. Finally, the total active and reactive powers  $P_{tot}, Q_{tot}$  exchanged with the grid:

$$P_{tot} = P_s + P_r \quad (10)$$

$$Q_{tot} = Q_s + Q_r \quad (11)$$

With vector control of the DFIG, the active and reactive powers are decoupled by orienting the rotor reference frame. The q-axis current component governs active power, while the d-axis component controls reactive power. To ensure precise dynamic and steady-state operation of the DFIG, the rotor dq current limits can be accurately calculated:

$$i_{qrmax} \approx -\frac{x_s + x_m}{x_m} P_{min} \quad (12)$$

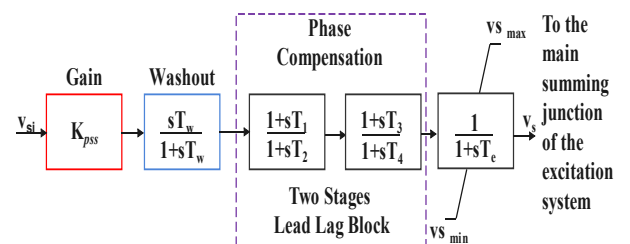


Fig. 2 Power system stabilizer type II block diagram.

$$i_{qr_{min}} \approx -\frac{x_s+x_m}{x_m} P_{max} \tag{13}$$

$$i_{dr_{max}} \approx -\frac{x_s+x_m}{x_m} Q_{min} - \frac{x_s+x_m}{x_m^2} \tag{14}$$

$$i_{dr_{min}} \approx -\frac{x_s+x_m}{x_m} Q_{max} - \frac{x_s+x_m}{x_m^2} \tag{15}$$

With  $P_{max}$ ,  $P_{min}$ ,  $Q_{max}$ , and  $Q_{min}$  are the DFIG's max-min active and reactive powers.

2.2 Power system stabilizer (PSS)

Negative damping in synchronous machines is primarily caused by delays in the field winding excitation. To mitigate this issue, Power System Stabilizers (PSS) are designed to counteract the destabilizing effect of these delays at critical frequencies between 1.0-2.0 Hz (Ramanujam, 2010). A typical configuration of a PSS is shown in Figure 2. The phase compensation block provides the necessary phase lead to the speed deviation signal. Practical PSS designs may utilize multiple lead-lag blocks for phase compensation. The washout block, with time constant  $T_w$  typically 0.1 to 20 seconds, prevents the PSS signal from introducing DC bias into the voltage regulator setpoint. The damping factor  $K_{pss}$  is a good measure of the damping amount. The anti-windup limiter controls the output signal  $v_s$  dynamics, which has a small time

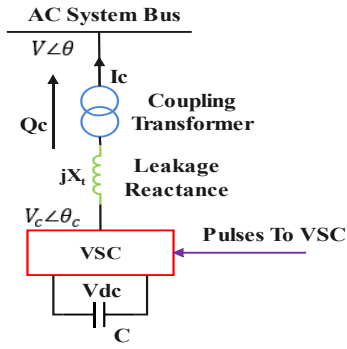


Fig. 3 STATCOM's basic model.

constant  $T_\epsilon = 0.001s$  (Milano, 2008). Note that the input signal in our study  $v_{si}$  is the rotor speed variation  $\Delta\omega$ . The PSS type II Differential-Algebraic Equations are given as follows:

$$\begin{aligned} \dot{v}_1 &= -(K_w v_{si} + v_1)/T_w \tag{16} \\ \dot{v}_2 &= ((1 - \frac{T_1}{T_2})(K_w v_{si} + v_1) - v_2)/T_2 \\ \dot{v}_3 &= ((1 - \frac{T_3}{T_4})(v_2 + (\frac{T_1}{T_2}(K_w v_{si} + v_1))) - v_3)/T_4 \end{aligned}$$

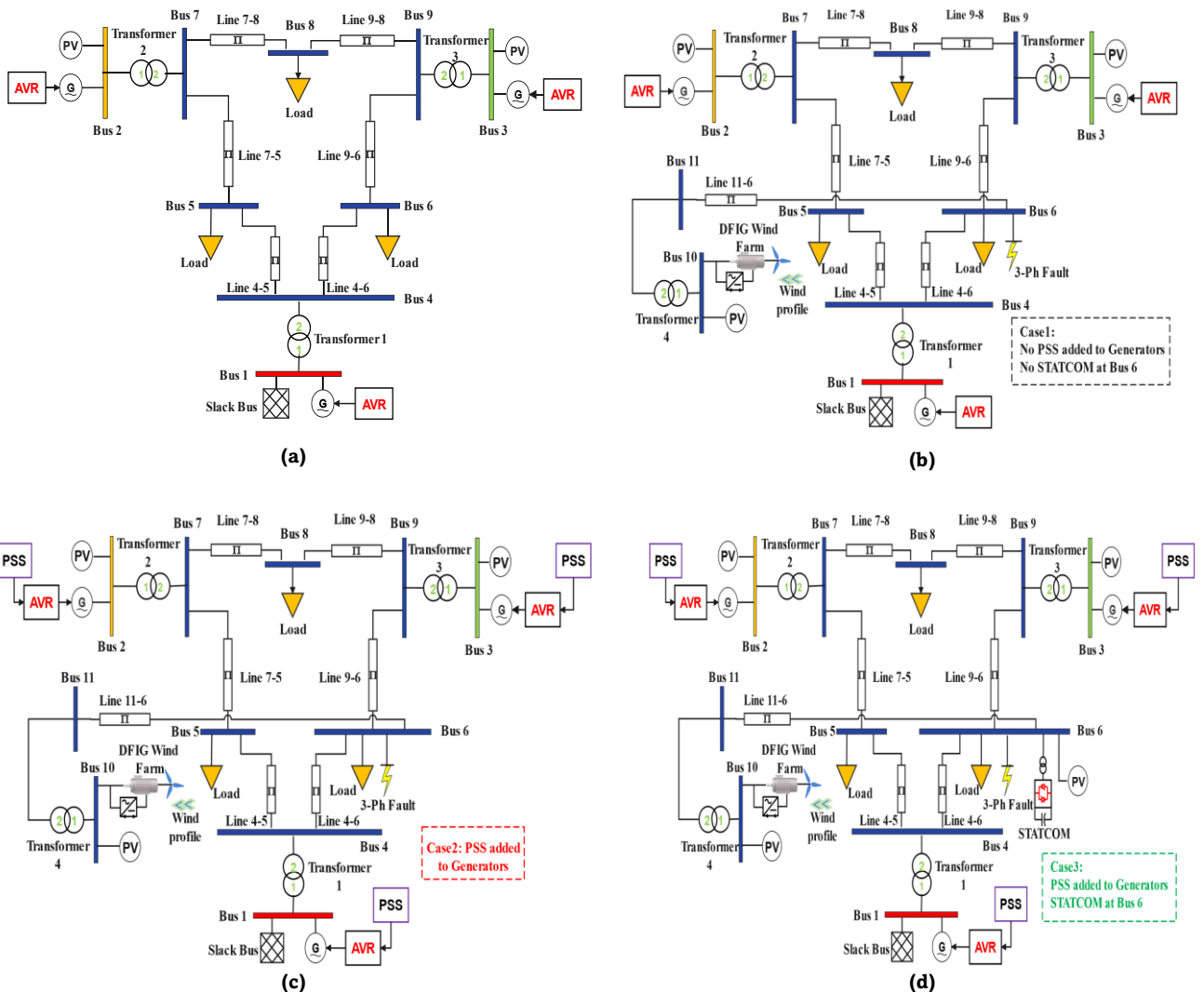


Fig. 4 WSCC 9 Bus test system in PSAT. (a) Original test system. (b) Modified test system (Case1). (c) Modified test system (Case2). (d) Modified test system (Case3).

$$\dot{v}_s = (v_3 + \frac{T_3}{T_4}(v_2 + (\frac{T_1}{T_2}(K_w v_{si} + v_1)) - v_s))/T_\epsilon$$

With  $T_1, T_2, T_3, T_4$  are the time constants for the 1<sup>st</sup>, 2<sup>nd</sup>, 3<sup>rd</sup> and the 4<sup>th</sup> stabilizers.  $v_1, v_2, v_3$  are the state variables.

### 2.3 Static synchronous compensator (STATCOM)

A static synchronous compensator (STATCOM) provides reactive power compensation by connecting in parallel with the power system. It utilizes solid-state switching converters supplied by capacitors or other energy storage elements (Hemeida *et al* 2018). Similar to a static VAR compensator (SVC), the STATCOM stabilizes transmission voltage through reactive shunt compensation. However, it can operate as either a voltage-sourced or current-sourced converter (Kothari & Nagrath, 2019). The STATCOM is versatile, capable of harmonic filtering, stability enhancement, and preventing voltage collapse. Integrating a STATCOM with wind generation can significantly improve system performance and stability (Hemeida *et al* 2018; Qiao *et al.*, 2009). Figure 3 illustrates the model of a STATCOM device.

To transmit reactive power from a STATCOM ( $Q_c$ ) to a power system, the device's voltage magnitude can be controlled using equation (17):

$$Q_c = \frac{V(V_c - V)}{X_t} \tag{17}$$

With  $V$  is the grid voltage,  $V_c$  representing STATCOM output voltage, and  $X_t$  the leakage reactance.

### 3. The simulation model description

Figure 4 summarizes the tested model configurations. The work utilizes the standard WSCC 9-bus power system model with a 100 MVA, 60 Hz base. Three synchronous generators are connected to buses 1, 2, and 3, with bus 1 as the slack bus and buses 2 and 3 as PV buses. Additionally, there are three PQ load buses interconnected at buses 5, 6, and 8, which connect to the rest of the system through six transmission lines, as manifested in Figure 4a. The specific system data used in the simulations is provided in detail in the Appendix.

The simulations were performed using the PSAT toolbox, a freely available MATLAB-based software for power system analysis (Milano, 2008). PSAT provides a comprehensive graphical interface and Simulink-based network editor, enabling convenient evaluation of system dynamics. The toolkit also features graphical user interfaces for constructing electrical schematics and multi-machine networks using pictorial blocks (Kumar *et al.*, 2020).

To evaluate the performance of the WSCC test system, a DFIG wind farm was integrated at bus 6 through a low impedance transmission line. Bus 6 was strategically chosen for the wind farm connection to effectively assess the overall system stability. The first test scenario subjected the reconfigured system to a three-phase fault at bus 6 without PSS and STATCOM controls (Figure 4b). The fault persisted for five cycles between  $t = 3$  s and  $t = 3.083$  s. The second scenario added PSS controllers to the AVR systems of all synchronous generators (Figure 4c). Finally, the third case incorporated a STATCOM device at bus 6. The last case configuration is illustrated in Figure 4d.

### 4. Simulation results and discussion

The trapezoidal integration method, widely recognized as a reliable and stable approach for diverse test scenarios, was utilized for the time-domain simulations. Notably, the upcoming subsection (4.1) will elaborate on the findings and results presented in Figures 5-9 and Table 1.

#### 4.1 Time-domain simulation results

This section evaluates the rotor angle  $\delta$ , angular velocity  $\omega$  of the synchronous generators, the DFIG's produced power  $P_{DFIG}$ , and the  $dq$  component of the rotor currents  $i_{dr}$  and  $i_{qr}$ . The three test cases are compared under wind power penetration levels of 0.2, 0.4, and 0.6 p.u. Table 1 summarizes the observed overshoots and undershoots for the simulated parameters.

##### a. Comparison with $P_{DFIG} = 0.2$ p.u. (all cases)

Large-disturbance rotor angle stability is a critical aspect of transient stability in power systems. It refers to the ability of synchronous generators to maintain synchronism and steady rotor angles when subjected to significant disturbances such as faults, sudden load changes, or transmission line outages. Rotor angle stability analysis focuses on controlling and minimizing rotor angle deviations during and after major system disturbances. Loss of synchronism between generators leads to unstable angular oscillations and system collapse (Prabha, 1994; Xu *et al.*, 2023).

The system as a whole appears stable, as plotted in Figs 5(a & b) and Figs 6(a & b). Figure 5a shows the power angles of the three generating units. For  $\delta_1$ , the no-control case has an overshoot of (+0.6546 rad, +37.5°) and undershoot of (-1.2213 rad, -70°) due to the slack bus response after the fault. The PSS, with high gain ( $K_w=50$ ) and fast time constant ( $T_w=0.1s$ ), rapidly applies corrective damping but initially overshoots (+0.73625 rad, +42.16°). However, it significantly reduces the undershoot by nearly 50% to (-0.68035 rad, -38.98°). With PSS

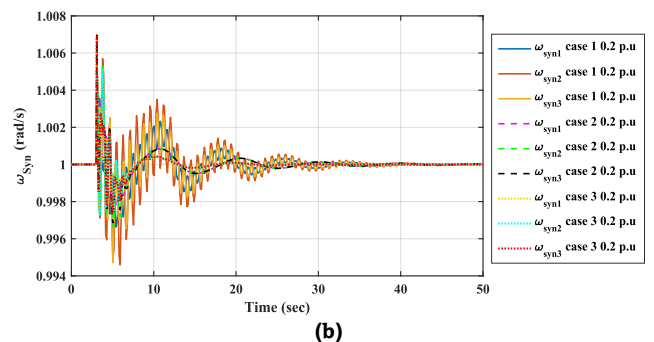
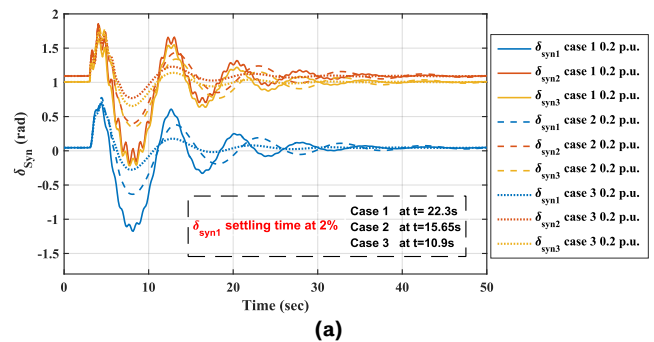
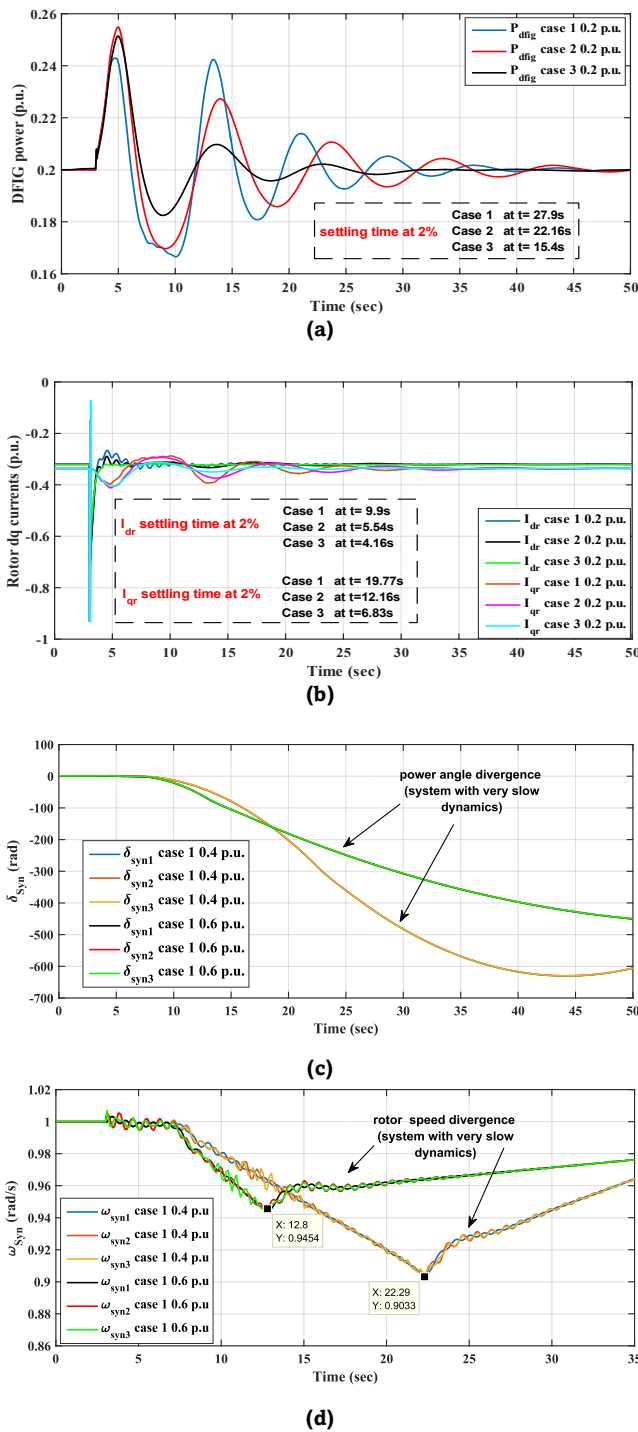


Fig. 5 Time-domain simulation results with ( $P_{DFIG} = 0.2$  p.u.). (a) Power angles, (b) Rotor angular speeds.



**Fig. 6** Time-domain simulation results (a) DFIG power with ( $P_{DFIG} = 0.2$  p.u.), (b) Rotor dq currents ( $P_{DFIG} = 0.2$  p.u.), (c) Power angles ( $P_{DFIG} = 0.4, 0.6$  p.u.), (d) Rotor angular speeds ( $P_{DFIG} = 0.4, 0.6$  p.u.).

and STATCOM, the overshoot further drops from  $+42.16^\circ$  to  $+38.29^\circ$ , while the undershoot is halved again from  $-38.98^\circ$  to  $-18.44^\circ$  with fastest 2% settling time of 10.9s. Regarding  $\delta_2$ , in the first case has a maximum overshoot of  $+43.8^\circ$  and undershoot of  $-73.4^\circ$  due to the high power output. The PSS slightly increases the overshoot to  $+44.06^\circ$  but reduces the undershoot by 45.6% to  $-39.93^\circ$ . With PSS and STATCOM, the overshoot decreases to  $+38.98^\circ$  and undershoot drops further by 53.46% to  $-18.55^\circ$ . As for  $\delta_3$ , the first case exhibits a maximum peak of  $(+0.627$  rad,  $+35.9^\circ)$ , and the lowest value reaches  $(-1.2248$  rad,  $-70.1^\circ)$ . These large angle deviations are

attributed to the third generator having the lowest inertia of 6.3 seconds. In spite of this, with the implementation of the PSS, it counterbalances the fast response of the low-inertia generator, resulting in a larger power angle deviation of  $+29.42^\circ$  ( $46.04^\circ$ ). Conversely, the lower band experiences a significant reduction of 44.62% to  $(-38.07^\circ)$ . Subsequently, both peaks are further lowered to  $42.16^\circ$  and  $-20.23^\circ$ , respectively, following the integration of the STATCOM.

Figure 5b shows the rotor angular velocities  $\omega_1$ ,  $\omega_2$ , and  $\omega_3$ . In case 1, the initial overshoot was  $+0.4\%$  ( $+0.24$  Hz) in  $\omega_1$  and  $+0.6\%$  ( $+0.36$  Hz) in  $\omega_2$ . However, in both the 2nd and the 3rd cases, overshoots noticeably reduced to  $+0.3\%$  ( $+0.18$  Hz) in  $\omega_1$  and  $+0.5\%$  ( $+0.30$  Hz) in  $\omega_2$ . For the minimum points,  $\omega_1$  undershoot declined by 32.3% to  $-0.23\%$  ( $-0.138$  Hz), while  $\omega_2$  declined by 37.04% to  $-0.34\%$  ( $-0.204$  Hz). Generator 1, with an inertia of 47s, had a slower, reduced response to disturbances, resulting in decreased overshoots. In contrast, Generator 2, with an inertia of 12.8s, exhibited a faster response with larger peaks. Regarding  $\omega_3$ , all cases had identical overshoots of  $+0.7\%$  (increase of 0.42Hz). The fast response of the 3rd generator with low inertia (6.2s) to faults provides insufficient time for the PSS/STATCOM to fully handle the initial overshoot. Yet, the undershoot experienced a considerable reduction of 40.74% from  $(-0.54\%, 0.334$ Hz) in the 1st case to  $(-0.32\%, 0.192$ Hz) in both subsequent cases. The three curves settle in around 32 seconds.

The three generators have inertias of 47.2, 12.8 and 6.2 seconds, respectively. Higher inertia provides for greater energy storage, damping, time constants, and synchronizing power. These factors reduce the sensitivity of rotor speed to disturbances, resulting in improved system stability and resilience against fluctuations in mechanical torque (Denholm et al., 2020, Eriksson et al., 2018). Moreover, Table 1 and Figs 5(a & b) demonstrate that even with  $+20$ MW wind penetration, the system can exhibit instability characterized by Low Frequency Oscillations (LFO) in both  $\delta$  and  $\omega$ . However, stability is significantly enhanced by the PSS/STATCOM combination, as evidenced by the reduced damped oscillations and peak values.

The plots 6(a & b) illustrate the DFIG's produced power  $P_{DFIG}$  and the dq rotor currents, correspondingly. Case 2 has the highest power peak at  $+27.4\%$ , corresponding to the maximum power angle deviations. Conversely, case 1 has the lowest undershoot of  $-16.75\%$ . With PSS and STATCOM in case 3, the overshoot reduces to  $+25.65\%$  while the undershoot substantially decreases to  $-8.8\%$ . The power signal shows effective damping characteristics over time. Notably, case 3 has the fastest 2% settling time of 15.4 seconds, indicating rapid dynamic response.

Based on equations (12-15), minimum undershoots of  $-0.7$  p.u. and  $-0.93$  p.u. are observed for  $i_{dr\_min}$  and  $i_{qr\_min}$  respectively in all cases at fault inception. In case 1,  $i_{dr}$  peaks at  $+17.01\%$  ( $Q_{min}$  of 0.0761 p.u.), while  $i_{qr\_max}$  reaches  $+56.21\%$ , increasing  $P_{DFIG}$  by  $+3.75\%$ . With PSS,  $i_{dr}$  drops by  $-42.05\%$  ( $Q_{min}$  of 0.0107 p.u.), confirming its indirect voltage control contribution. Meanwhile,  $i_{qr\_max}$  peaks at  $+56.63\%$ , reflecting the  $+3.75\%$   $P_{DFIG}$  rise. The peaks occur at  $t=4.54$ s for  $i_{dr\_max}$  and  $t=3.121$ s for  $i_{qr\_max}$ . In case 3,  $i_{dr}$  substantially decreases by 76.38% to 2.33% ( $Q_{min}$  of  $-0.0105$  p.u.), indicating reactive power absorption. This significant reduction results from the additional reactive support by the STATCOM, further evidenced by the decreased over-voltage at bus 10 in Table 2. Conversely,  $i_{qr}$  increases by 38.41%, representing a 4% rise in wind farm output. Alongside the power boost, case 3 has the shortest 2% settling times for both currents at  $t=4.16$ s and  $t=8.88$ s for  $i_{dr}$  and  $i_{qr}$  respectively.

**Table 1**  
Overshoots and undershoots of  $\delta_{syn}$ ,  $\omega_{syn}$ ,  $P_{DFIG}$ ,  $i_{dr}$ ,  $i_{qr}$ ,  $I_{statcom}$  for all cases.

	Case 1 (No PSS/No STATCOM)			Case 2 (Only PSS)			Case 3 (PSS + STATCOM)		
	0.2 p.u.	0.4 p.u./ 0.6 p.u.	0.2 p.u.	0.4 p.u.	0.6 p.u.	0.2 p.u.	0.4 p.u.	0.6 p.u.	
$\delta_1$ (rad)	0.6546 (+37.5 °)	Instable	0.73625 (+42.16 °)	0.6574 (+36.06 °)	0.5314 (+30.44 °)	0.66815 (+38.29 °)	0.5406 (+30.97 °)	0.4399 (+25.18 °)	
	-1.2213 (-70 °)		-0.68035 (-38.98 °)	-0.5858 (-33.56 °)	-0.5235 (-29.98 °)	-0.32185 (-18.44 °)	-0.2767 (-15.85 °)	-0.2748 (-15.75 °)	
$\delta_2$ (rad)	0.764 (+43.8 °)	Instable	0.769 (+44.06 °)	0.698 (+40 °)	0.624 (+35.72 °)	0.68 (+38.98 °)	0.59 (+33.85 °)	0.518 (+29.68 °)	
	-1.2826 (-73.4 °)		-0.6974 (-39.93 °)	-0.6011 (-34.44 °)	-0.5845 (-33.47 °)	-0.3238 (-18.55 °)	-0.2798 (-16.03 °)	-0.2645 (-15.17 °)	
$\delta_3$ (rad)	0.627 (+35.9 °)	Instable	0.803 (+46.04 °)	0.668 (+38.27 °)	+0.631 (+36.14 °)	0.737 (+42.16 °)	0.63 (+36.14 °)	0.539 (+30.9 °)	
	-1.2248 (-70.1 °)		-0.6641 (-38.07 °)	-0.501 (-28.7 °)	-0.4346 (-24.89 °)	-0.3531 (-20.23 °)	-0.2856 (-16.36 °)	-0.2701 (-15.47 °)	
$\omega_1$ (rad/s)	+0.4%(+0.24Hz)	Instable	+0.3%(+0.18Hz)	+0.3%(+0.18Hz)	+0.3%(+0.18Hz)	+0.3%(+0.18Hz)	+0.3%(+0.18Hz)	+0.3%(+0.18Hz)	
	-0.34%(-0.204Hz)		-0.23%(-0.138Hz)	-0.21%(-0.126Hz)	-0.22%(-0.132Hz)	-0.21%(-0.126Hz)	-0.21%(-0.126Hz)	-0.18%(-0.108Hz)	
$\omega_2$ (rad/s)	+0.6%(+0.36Hz)	Instable	+0.5%(+0.36Hz)	+0.5%(+0.3Hz)	+0.5%(+0.3Hz)	+0.5%(+0.3Hz)	+0.5%(+0.3Hz)	+0.5%(+0.3Hz)	
	-0.54%(-0.324Hz)		-0.34%(-0.204Hz)	-0.37%(+0.222Hz)	-0.39%(-0.234Hz)	-0.33%(-0.198Hz)	-0.37%(-0.222Hz)	-0.35%(-0.21Hz)	
$\omega_3$ (rad/s)	+0.7%(+0.42Hz)	Instable	+0.7%(+0.42Hz)	+0.7%(+0.42Hz)	+0.7%(+0.42Hz)	+0.7%(+0.42Hz)	+0.7%(+0.42Hz)	+0.7%(+0.42Hz)	
	-0.54%(-0.324Hz)		-0.32%(-0.192Hz)	-0.3%(-0.18Hz)	-0.31%(-0.186Hz)	-0.31%(-0.186Hz)	-0.3%(-0.18Hz)	-0.21%(-0.126Hz)	
$P_{DFIG}$ (p.u.)	+21.5%	Instable	+27.4%	+12.75%	+7.83%	+25.65%	+10.92%	+6.32%	
	-16.75%		-16.05%	-5.6%	-3.78%	-8.8%	-3.475%	-2.32%	
$i_{dr}$ (p.u.)	+17.01%	Instable	+9.86%	+7.9%	+5%	+2.33%	+0.37%	+0.42%	
	$i_{dr_{min}}$		$i_{dr_{min}}$	$i_{dr_{min}}$	$i_{dr_{min}}$	$i_{dr_{min}}$	$i_{dr_{min}}$	$i_{dr_{min}}$	
$i_{qr}$ (p.u.)	+56.21%	Instable	+56.63%	+19.3%	+8.53%	+78.38%	+32%	+16.81%	
	$i_{qr_{min}}$		$i_{qr_{min}}$	$i_{qr_{min}}$	$i_{qr_{min}}$	$i_{qr_{min}}$	$i_{qr_{min}}$	$i_{qr_{min}}$	
$I_{Statcom}$ (p.u.)	—	—	—	—	—	$i_{statcom_{max}}$ -0.3143	$i_{statcom_{max}}$ -0.3105	$i_{statcom_{max}}$ -0.2932	

*b. Comparison with  $P_{DFIG} = 0.4$  p.u., 0.6 p.u. (case1)*

Figures 6(c & d) and Figs 7(a & b) show that case 1 becomes unstable at  $t = 22.4s$  and  $t = 12.8s$  for 0.4 p.u. and 0.6 p.u. wind penetration, in turn. Specifically, at 0.6 p.u., voltages on buses 5, 6, 8, 10, and 11 undergo catastrophic failure. The DFIG rotor currents reach minimum limits, triggering the speed and voltage controller anti-windup mechanisms to prevent over-currents in the converters and maintain powers and currents within limits. However, the generator power angles still diverge and rotor speeds display completely undamped behavior with very slow dynamic divergence.

*c-Comparison with  $P_{DFIG} = 0.4$  p.u. (case 2 and 3)*

Figures 7(c, d, & e), and 8a depict demonstrate system stability under the specified conditions. Compared to 0.2 p.u., adding PSS in case 2 decreases the power angle overshoots by 14.5%, 9.2%, and 16.86% for  $\delta_1$ ,  $\delta_2$ , and  $\delta_3$  respectively, as shown in Fig. 7c and Table 1. This is attributed to the extra 0.53s inertia from the DFIG. With PSS and STATCOM damping in case 3, the angles further reduce to 30.97°, 33.85°, and 36.14°, changed by -14.12%, -15.38%, and -5.57% correspondingly. Regarding undershoots, case 2 has lower values versus case 1: -13.87% for  $\delta_1$ , -13.75% for  $\delta_2$ , and -24.6% for  $\delta_3$ , unlike at 20 MW. Moreover, case 3 optimizes these minimums substantially with declines of -52.7%, -53.4%, and -42.9% for the angles respectively. Case 3 also exhibits the fastest 2% settling time of 13.05 seconds.

For rotor speeds  $\omega_1$ ,  $\omega_2$ , and  $\omega_3$ , cases 2 and 3 have similar overshoots of +0.3%, +0.5%, and +0.7% and undershoots of -0.21%, -0.37%, and -0.3% respectively. However, compared to 0.2 p.u., the undershoots in case 2 decrease by -8.70% for  $\omega_1$  and -6.25% for  $\omega_3$ , while  $\omega_2$  increases by +8.82% due to the

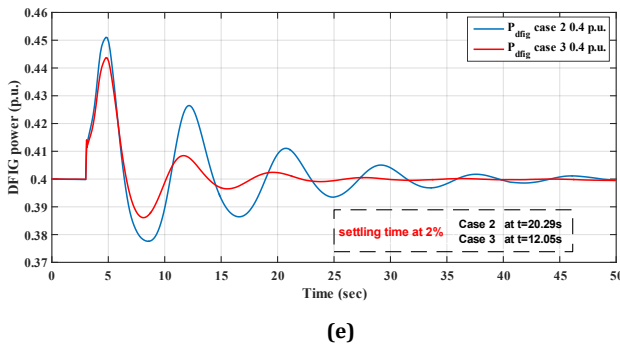
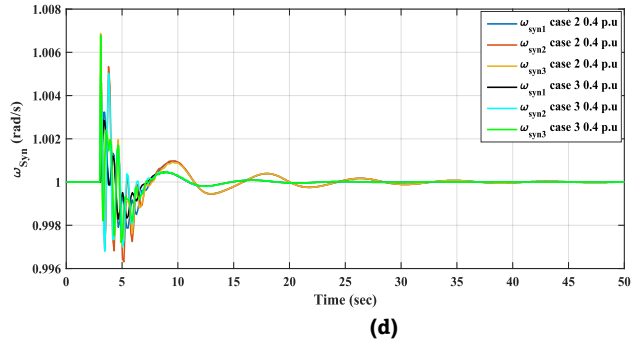
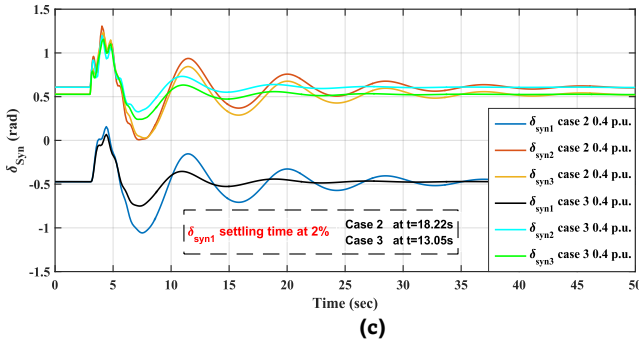
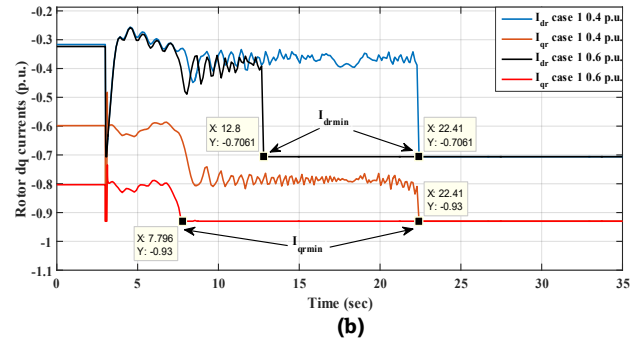
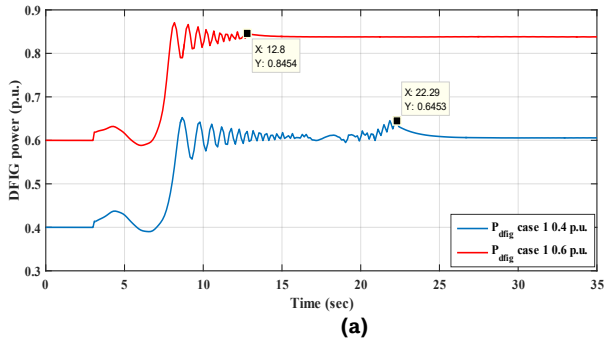
DFIG's added 0.53s inertia influencing system dynamics. The three units resynchronize in approximately 14.2 seconds, as shown (Fig 7d).

The generated power and the  $dq$  rotor currents are pictured in Figures 7e and 8a, in that order. Adding the STATCOM in case 3 reduces the power peaks from (+12.75%, -5.6%) in case 2 to (+10.92%, -3.475%), decreasing them by -14.35% and -37.95% respectively, with a 2% settling time of 12.05s. As stated before,  $i_{dr_{max}}$  and  $i_{qr_{min}}$  are the minimum points. In case 2,  $i_{dr}$  peaks at +7.9% ( $Q_{min}$  of -0.0511 p.u.), while max  $i_{qr}$  reaches +19.3%, increasing turbine power by +3.225%. Versus case 1,  $i_{dr}$  shows a smaller +0.37% rise ( $Q_{min}$  of -0.0236 p.u.), while  $i_{qr}$  exhibits a larger +32% growth corresponding to a +2.85% power increase. The peaks occur at  $t=4.5s$  for  $i_{dr}$  and  $t=3.128s$  for  $i_{qr}$ . The currents settle to 2% pre-fault value at  $t=4.54s$  and  $t=6.04s$ .

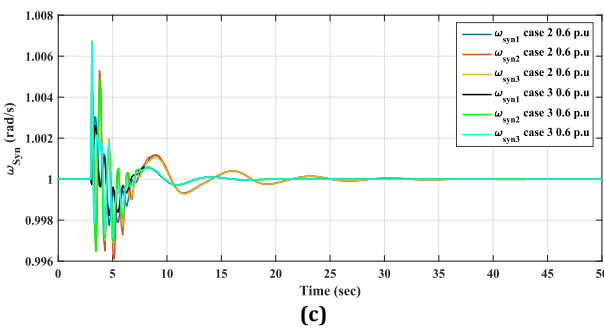
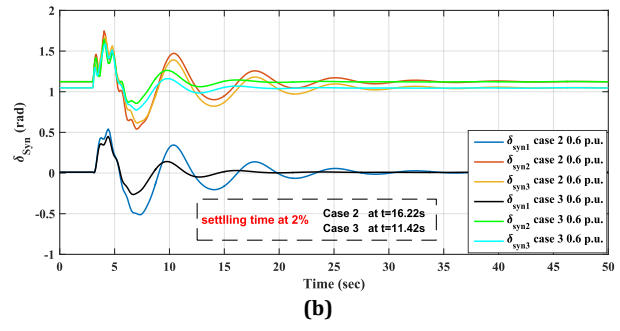
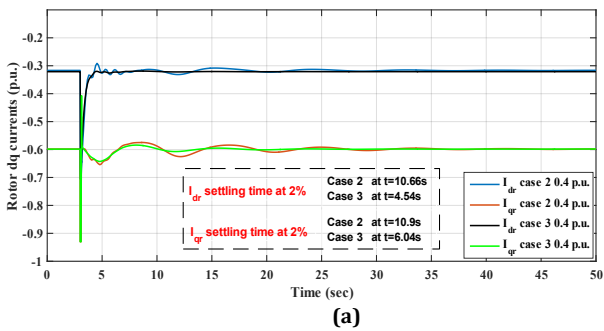
*d-Comparison with  $P_{DFIG} = 0.6$  p.u. (case 2 and 3)*

Figure 8b plots the power angles of the three generators. Compared to 0.4 p.u., case 2 shows reduced overshoot peaks of -15.59%, -23.20%, and -5.58% for  $\delta_1$ ,  $\delta_2$ , and  $\delta_3$  in turn, while the minimums decrease by -10.63%, 2.82%, and 13.2% respectively. In case 3, overshoots are further lowered by -17.28%, -3.39%, and -14.56%, and minimums are optimized with reductions of -47.47%, -55.16%, and -37.94% for the angles, reaching steady state after 27s. These results validate the enhanced system stability provided by additional damping support from the wind generation and controllers. Prior work by (Edrah et al., 2015; He et al., 2022; Shahgholian & Izadpanahi, 2016) supports utilizing wind farms for stability improvement.

Table 1 and Figure 8c show identical rotor velocity overshoots for both cases 2 and 3. However, the minimums



**Fig. 7** Time-domain simulation results (a) DFIG power with ( $P_{DFIG} = 0.4, 0.6$  p.u.), (b) Rotor dq currents ( $P_{DFIG} = 0.4, 0.6$  p.u.), (c) Power angles ( $P_{DFIG} = 0.4$  p.u.), (d) Rotor angular speeds ( $P_{DFIG} = 0.4$  p.u.), (e) DFIG power ( $P_{DFIG} = 0.4$  p.u.).



**Fig. 8** Time-domain simulation results (a) Rotor dq currents ( $P_{DFIG} = 0.4$  p.u.), (b) Power angles ( $P_{DFIG} = 0.6$  p.u.), (c) Rotor angular speeds ( $P_{DFIG} = 0.6$  p.u.).

decrease by -18.18%, -10.26%, and -32.26% with the STATCOM addition in case 3. Compared to 0.4 p.u., the PSS and STATCOM

combination reduces the power peaks from (+7.83%, -5.6%) in case 2 to (+6.32%, -3.475%) in case 3, decreasing them by -

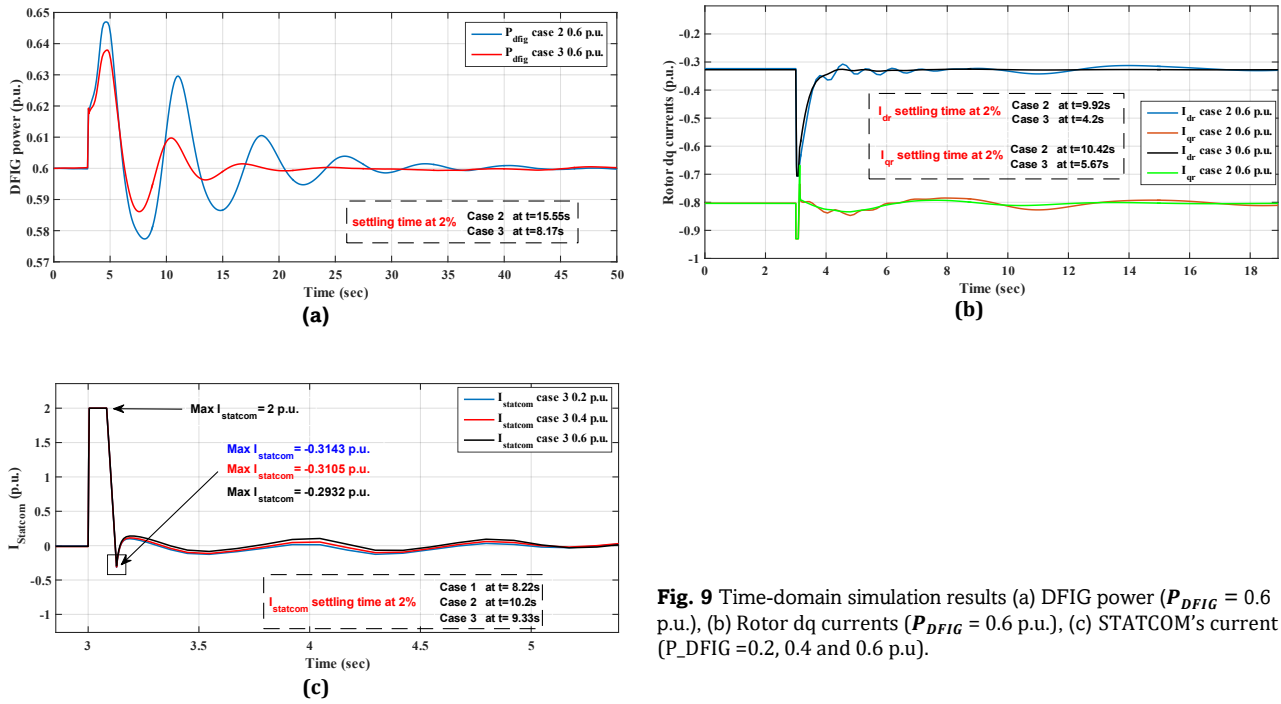


**Fig. 9** Time-domain simulation results (a) DFIG power ( $P_{DFIG} = 0.6$  p.u.), (b) Rotor dq currents ( $P_{DFIG} = 0.6$  p.u.), (c) STATCOM's current ( $P_{DFIG}=0.2, 0.4$  and  $0.6$  p.u.).

**Table 2**

Bus voltage  $V_1, V_2, V_3, V_6, V_{10}$  (at  $t=3.5s$ )

	Case 1 (No PSS/No STATCOM)			Case 2 (Only PSS)			Case 3 (PSS + STATCOM)		
	0.2 p.u.	0.4 p.u.	0.6 p.u.	0.2 p.u.	0.4 p.u.	0.6 p.u.	0.2 p.u.	0.4 p.u.	0.6 p.u.
$V_1$ (p.u.)	+1.44%(1.04)	+1.54%(1.04)	+1.73%(1.04)	<b>+1.92%</b> (1.04)	+1.44%(1.04)	+0.87%(1.04)	+1.54%(1.04)	+1.06%(1.04)	<b>+0.48%</b> (1.04)
$V_2$ (p.u.)	+1.36%(1.025)	+1.46%(1.025)	+1.56%(1.025)	+0.78%(1.025)	+0.49%(1.025)	+0.29%(1.025)	+0.59%(1.025)	+0.49%(1.025)	<b>+0.10%</b> (1.025)
$V_3$ (p.u.)	+1.07%(1.025)	+1.17%(1.025)	<b>+1.27%</b> (1.025)	-0.78%(1.025)	-0.98%(1.025)	-1.07%(1.025)	-1.17%(1.025)	-1.27%(1.025)	<b>-1.46%</b> (1.025)
$V_6$ (p.u.)	+1.95%(1.027)	+2.24%(1.027)	<b>+2.43%</b> (1.027)	+1.56%(1.027)	+1.46%(1.027)	+1.17%(1.027)	+0.19%(1.027)	+0.19%(1.027)	<b>+0.1%</b> (1.027)
$V_{10}$ (p.u.)	+3.01%(1.03)	<b>+3.01%</b> (1.03)	<b>+3.11%</b> (1.03)	+2.43%(1.03)	+2.43%(1.03)	+2.33%(1.03)	+1.17%(1.03)	+1.17%(1.03)	<b>+1.17%</b> (1.03)

**Table 3**

Bus voltage  $V_4, V_2, V_5, V_7, V_8, V_9, V_{11}$  (at  $t=3.5s$ )

	Case 1 (No PSS/No STATCOM)			Case 2 (Only PSS)			Case 3 (PSS + STATCOM)		
	0.2 p.u.	0.4 p.u.	0.6 p.u.	0.2 p.u.	0.4 p.u.	0.6 p.u.	0.2 p.u.	0.4 p.u.	0.6 p.u.
$V_4$ (p.u.)	<b>+2.52%</b> (1.03)	+1.94%(1.03)	+2.04%(1.03)	+2.14%(1.03)	+2.14%(1.03)	+2.04%(1.03)	+0.78%(1.03)	<b>+0.78%</b> (1.03)	+0.87%(1.03)
$V_5$ (p.u.)	<b>+5.05%</b> (0.9988)	+5.12%(0.9988)	<b>+5.23%</b> (0.9988)	+5.16%(0.9988)	+4.64%(0.9988)	+4.13%(0.9988)	+4.32%(0.9988)	+3.92%(0.9988)	<b>+3.53%</b> (0.9988)
$V_7$ (p.u.)	-1%(1.027)	-0.78%(1.027)	<b>-0.68%</b> (1.027)	-1.07%(1.027)	-1.46%(1.027)	-1.85%(1.027)	-1.66%(1.027)	-1.95%(1.027)	<b>-2.34%</b> (1.027)
$V_8$ (p.u.)	+2.36%(1.018)	+2.46%(1.018)	<b>+2.55%</b> (1.018)	+1.77%(1.018)	+1.47%(1.018)	+1.28%(1.018)	+1.38%(1.018)	+1.18%(1.018)	<b>+0.88%</b> (1.018)
$V_9$ (p.u.)	-0.29%(1.035)	-0.19%(1.035)	<b>-0.1%</b> (1.035)	-1.16%(1.035)	-1.45%(1.035)	<b>-1.64%</b> (1.035)	-1.64%(1.035)	-1.74%(1.035)	<b>-2.03%</b> (1.035)
$V_{11}$ (p.u.)	+1.65%(1.032)	+2.62%(1.032)	<b>+2.81%</b> (1.032)	+0.29%(1.032)	+0.1%(1.032)	+0%(1.032)	-0.52%(1.032)	-0.38%(1.032)	<b>-0.58%</b> (1.032)

19.28% and -38.62% respectively. This also represents respective declines of -42.01% and -49.92% versus case 2. Additionally, the 2% settling time for power shortens to 8.17s faster, as depicted in plot 9a.

Likewise, Figure 9b conveys the DFIG's rotor currents. In case 2,  $i_{dr\_max}$  reaches +5% ( $Q_{min} \approx 0.0573$  p.u.), while  $i_{qr}$  is +8.53%, increasing  $P_{DFIG}$  by +3.1%. However, in case 3,  $i_{dr}$  peaks at +0.42% ( $Q_{min} \approx -0.0115$  p.u.), while  $i_{qr\_max}$  rises to +16.81%, reflecting a +2.93%  $P_{DFIG}$  increment per equation 12. The peaks occur at  $t=4.55s$  and  $t=3.128s$  for  $i_{dr}$  and  $i_{qr}$  consecutively. Notably, case 3 has the fastest settling times at  $t=4.2s$  and  $t=5.67s$  for the  $dq$  currents.

Figure 9c exhibits the STATCOM currents. Despite being a current source, the STATCOM controls voltage while providing reactive power. During the  $t=3s$  fault,  $V_6$  drops -98.5% to 0.01154 p.u. The STATCOM responds by generating  $Q_{statcom}=2.7$  Mvar at maximum current to restore  $V_6$ . After fault clearance at  $t=3.128s$ , it absorbs (-28.4 Mvar), (-30.1 Mvar), and (-30.4 Mvar) for 60 MW, 40 MW, and 0.2 p.u.  $P_{DFIG}$  levels respectively to regulate  $V_6$ . Thus, higher wind penetration leads to less reactive power absorption post-fault.  $V_6$  is maintained at 1.027 p.u. at steady state regardless of wind level. The currents settle in approximately 10.5 seconds.

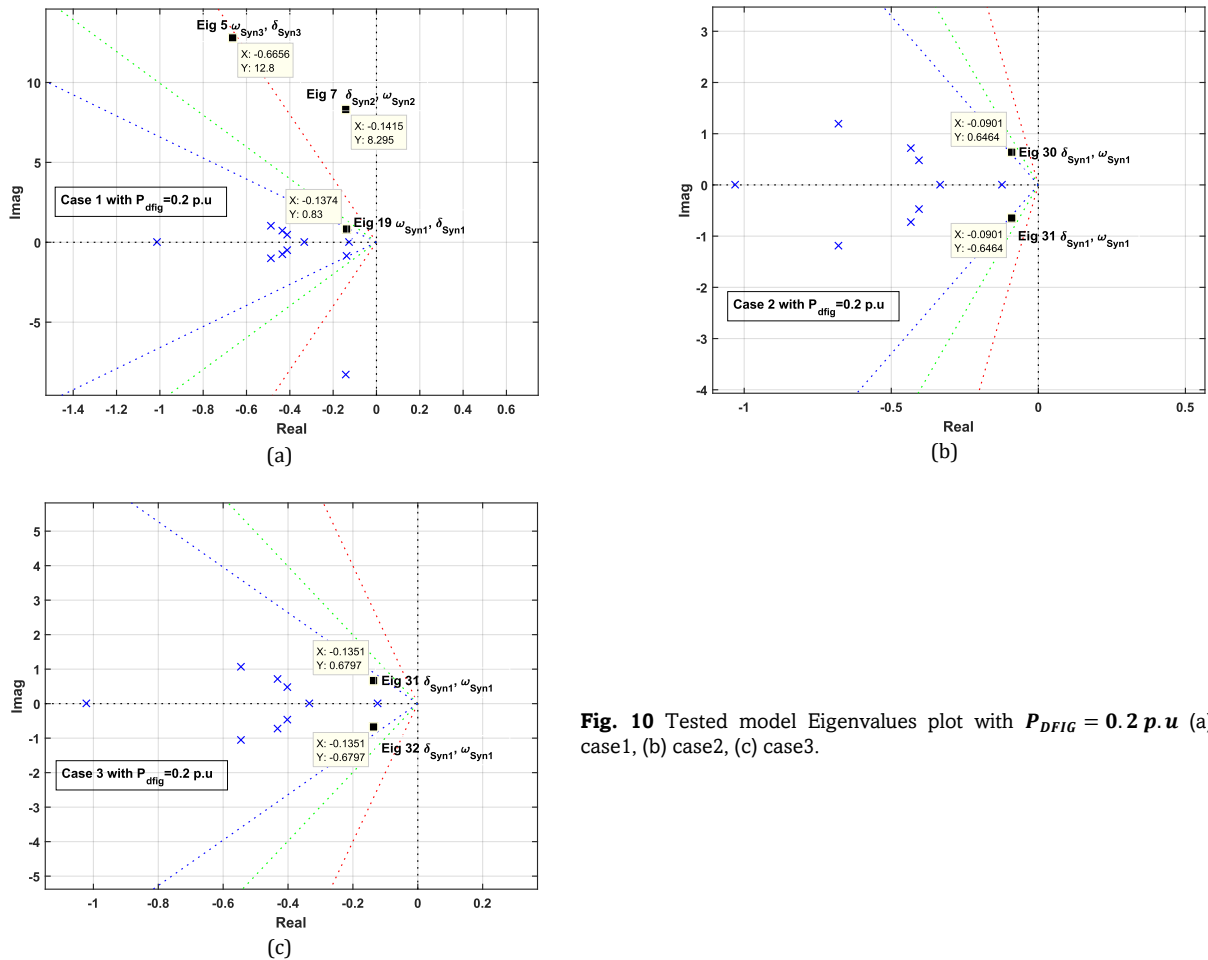


Fig. 10 Tested model Eigenvalues plot with  $P_{DFIG} = 0.2 p.u$  (a) case1, (b) case2, (c) case3.

4.2 Load flow results

Assessing voltage stability is crucial for power system management, as it ensures optimal voltage levels are maintained during normal operation and disturbances. This is vital for reliable functioning of the grid, requiring continuous monitoring (Carson et al., 1994). Considering the three test cases, Tables 2 and 3 comprehensively summarize the load flow results, specifically showcasing the voltage values at buses 1 through 11. These provide insights into the voltage profiles within the system. The 0.2 p.u. wind case without controllers (bracketed values in Tables 2 & 3) is used as a reference to examine the impact of increased wind injection and controller cooperation on dynamic voltage response. With similar PSS and STATCOM time constants ( $T_w = T_r = 0.1s$ ),  $t=3.5s$  is selected to evaluate steady-state bus voltages, allowing  $\sim 0.5s$  settling time. A  $\pm 10\%$  tolerance in voltages is permitted. Specifically, the post-fault cleared voltages offer visibility into short-term dynamic response. Key insights include (Adebayo & Sun, 2017; Balasubramanian & Singh, 2011; Ma et al., 2017):

- Detecting dangerous electromechanical oscillations through sustained voltage swings at certain buses, indicating poorly damped modes requiring improved controls.
- Identifying areas slow to recover voltage, guiding placement of fast dynamic reactive reserves to support at-risk regions.
- Revealing dangerously depressed voltage levels right after fault clearance that could precipitate delayed instability without rapid correction.

- Verifying performance of voltage regulators, PSS, STATCOMs, and generator reactive power in quickly restoring voltages, with deficiencies corrected
- Validating short-term transient stability margins by checking for dangerously low voltages that could signify insufficient margins.

a. Case 1

Based on Tables 2&3, with a wind integration of 0.2 p.u., the bus voltages (1, 2, 3, 6, and 10) exhibit transient overvoltage in a range of +1% to +3% due to the system's natural response to the sudden change in load.

Furthermore, at 0.2 p.u., Bus 5 (heaviest load) has the highest voltage surge of +5.05%, while  $V_4$  reduces by -1%. With 0.4 p.u. wind, Bus 10 maintains a +3% rise,  $V_4$  drops 0.58%, and Buses 7 and 9 increase by 0.22% and 0.1% respectively. The other buses show smaller 0.10-0.98% changes. However, at  $t=22.41s$ , voltage instability occurs with failures predominantly at load Buses 5, 6, 8 and DFIG Buses 10, 11, due to their low impedance connections to the faulty location.

Similarly, with 0.6 p.u. wind, voltages surge a further 0.1-0.2% at  $t=3.5 s$  across all buses. The largest increases of +0.19% occur at  $V_1, V_6,$  and  $V_{11}$ . However, at  $t=12.8s$ , severe voltage instability occurs with catastrophic violations at load buses 5, 6, 8 and DFIG buses 10, 11. This result from the large reactive current rush during the fault leading to sustained low frequency oscillations and complete transient voltage collapse. The results highlight the critical need to prioritize voltage regulation as wind integration increases, which is crucial for maintaining power system stability and reliability.

**Table 4**  
Overall Power Statistics.

	Case 1 (No PSS/No STATCOM)			Case 2 (Only PSS)			Case 3 (PSS + STATCOM)		
	0.2 p.u.	0.4 p.u.	0.6 p.u.	0.2 p.u.	0.4 p.u.	0.6 p.u.	0.2 p.u.	0.4 p.u.	0.6 p.u.
$P_{gen}$ (p.u.)	3.1953	3.1961	3.1986	3.1953	3.1961	3.1986	3.1953	3.1961	3.1986
$Q_{gen}$ (p.u.)	0.0402	0.05017	0.08459	0.0402	0.05017	0.08459	0.03657	0.0471	0.08133
$P_{load}$ (p.u.)	3.15	3.15	3.15	3.15	3.15	3.15	3.15	3.15	3.15
$Q_{load}$ (p.u.)	1.15	1.15	1.15	1.15	1.15	1.15	1.15	1.15	1.15
$P_{loss}$ (p.u.)	0.04526	0.04605	0.0486	0.04526	0.04605	0.0486	0.04527	0.04605	0.0486
$Q_{loss}$ (p.u.)	-1.1098	-1.0998	-1.0654	-1.1098	-1.0998	-1.0654	-1.1096	-1.0988	-1.0645

**Table 5**  
Linear value analysis of the tested system.

Cases	Eig.n°	Most associated states	Real part	Img part	freq	Damping ratio%	Mode/Remarks
Case 1: $P_{DFIG} = 0.2p.u.$	5-6	omega_Syn_3, delta_Syn_3	-0.66556	±12.8017	2.0402	+5.2	Local mode 3
	7-8	delta_Syn_2, omega_Syn_2	-0.14151	±8.2949	1.3204	+1.7	Inter area mode (Gen2, Gen1)
	19-20	omega_Syn_1, delta_Syn_1	-0.13735	±0.83001	0.1339	+16.5	
Case 2: $P_{DFIG} = 0.2p.u.$	30-31	delta_Syn_1, omega_Syn_1	-0.0901	±0.64637	0.10387	+13.93	Local mode 1
Case 3: $P_{DFIG} = 0.2p.u.$	31-32	delta_Syn_1, omega_Syn_1	-0.13512	±0.67969	0.11029	+19.8	Local mode 1
Case 1: $P_{DFIG} = 0.4p.u.$	4-5	omega_Syn_3, delta_Syn_3	-0.88353	±11.7908	1.8818	+7.49	Local mode 3
	6-7	omega_Syn_2, delta_Syn_2	-0.18133	±7.6103	1.2116	+2.38	Inter area mode (Gen2, Gen1)
	16	delta_Syn_1, omega_Syn_1	0.00011	0.1465	0.02332	/	
	17	omega_Syn_1, delta_Syn_1	0.00011	-0.1465	0.02332	/	Marginal instability
Case 2: $P_{DFIG} = 0.4p.u.$	30-31	delta_Syn_1, omega_Syn_1	-0.08991	±0.64547	0.11909	+13.93	Local mode 1
Case 3: $P_{DFIG} = 0.4p.u.$	31-32	delta_Syn_1, omega_Syn_1	-0.16356	±0.78322	0.12734	+20.88	Local mode 1
Case 1: $P_{DFIG} = 0.6p.u.$	4-5	delta_Syn_3, omega_Syn_3	-0.86609	±11.7848	1.8807	+7.43	Local mode 3
	6-7	omega_Syn_2, delta_Syn_2	-0.17429	±7.5708	1.2052	+2.3	Inter area mode (Gen2, Gen1)
	16	delta_Syn_1, omega_Syn_1	5e-05	0.09393	0.01495	/	
	17	delta_Syn_1, omega_Syn_1	5e-05	0.09393	0.01495	/	Marginal instability
Case 2: $P_{DFIG} = 0.6p.u.$	30-31	delta_Syn_1, omega_Syn_1	-0.13807	±0.85751	0.13823	+16.12	Local mode 1
Case 3: $P_{DFIG} = 0.6p.u.$	28-29	omega_Syn_1, delta_Syn_1	-0.40367	±1.1875	0.19962	+34	Local mode 1

*b. comparison between Case 2 and 3*

*1- with  $P_{DFIG} = 0.2 p.u$*

In Case 3, adding a STATCOM provided enhanced voltage regulation compared to just PSS control in Case 2, with improvements of 1.36%, 0.84%, 1.37% and 1.26% at Buses 4, 5, 6 and 10, respectively. However, minor voltage drops between 0.29-0.59% occurred at Buses 3, 7, 9 and 11. The coordinated PSS and STATCOM yielded overall positive, though not universal, voltage profile enhancements at 0.2 p.u. wind. The most substantial regulation improvements occurred near the STATCOM location, demonstrating its local area voltage support capabilities.

*2- with  $P_{DFIG} = 0.4 p.u$*

Under 40% of wind invasion, the coordinated PSS and STATCOM controls in Case 3 provided appreciable voltage regulation improvements at several buses versus sole PSS control in Case 2. However, select buses exhibited minor degradation versus Case 2, denoting opportunities for further

optimization. Specifically, adding the STATCOM yielded notable gains of 1.36% at Bus 4, 0.72% at Bus 5, 1.27% at Bus 6, and 1.26% at Bus 10 over PSS alone. Conversely, regulation dropped 0.29% at Bus 3, 0.49% at Bus 7, 0.29% at Bus 9, and 0.14% at Bus 11 compared to Case 2. Nonetheless, the multi-device strategy facilitated considerable 0.29-1.36% enhancements at Buses 1, 4, 5, 6, 8, and 10 at 0.4 p.u. wind. Additional assessment of techniques minimizing deviations at specific buses remains vital for optimizing voltage profiles.

*3- with  $P_{DFIG} = 0.6 p.u$*

At 0.6 p.u. wind, adding a STATCOM in Case 3 provided appreciable voltage regulation improvements at several buses compared to just PSS control in Case 2. Notable gains occurred at Buses 1, 2, 4, 5, 6, 8 and 10. However, degradation materialized at Buses 3, 7, 9, and 11. While beneficial overall, further refinement and coordination of the PSS and STATCOM controllers remains vital for achieving consistent voltage profile enhancements across all buses, given the variability observed under 0.6 p.u. renewable integration.

Table 4 provides a clear and concise presentation of the power data, including total active and reactive generated power, load, and losses. It offers a comprehensive overview of the power flow within the system, enabling a detailed analysis of the different components involved Table 4 clearly and concisely summarizes the power flow data, including total active and reactive generation, load, and losses. It provides a comprehensive overview enabling detailed analysis. For power losses, cases 1 and 2 are identical since PSSs do not directly impact them. In both, at 0.2 p.u. wind, reactive power loss is highest at -1.1098 p.u. due to the low  $Q_{gen}$  0.22885 p.u. from units 1 and 2, while the DFIG and unit 3 absorb 0.18865 p.u.

As wind increases to 0.4 p.u., the reactive power loss shrinks to -1.0998 p.u., due to higher 0.24311 p.u.  $Q_{gen}$  and 0.19224 p.u. absorption. At 60 MW DFIG output,  $Q_{loss}$  further reduces to -1.0654 p.u. with 0.26845 p.u.  $Q_{gen}$  and 0.18385 p.u. absorption.

Furthermore, from 0.2 to 0.6 p.u.  $P_{DFIG}$  in Case 3, reactive power loss drops from -1.1096 p.u. to -1.0645 p.u., a 4.06% reduction. Higher DFIG output leads to increased reactive absorption, as the DFIG operates at a lagging power factor as output rises. However, the STATCOM can increase its output to compensate. This additional STATCOM contribution helps maintain low reactive power losses as wind penetration increases (Qiao et al., 2009, Shahgholian & Izadpanahi, 2016).

4.3 Eigenvalue analysis

This study employed the eigenvalue analysis tool that is incorporated in the PSAT Toolbox. A total of 39 states were initiated and analyzed, which comprise 13 complex pairs.

Figures 10-12 present the eigenvalues plots regarding the tested system. Based on the results of the eigenvalue analysis, Table 5 presents further details on the dominant oscillation modes. Participation factors were utilized to identify the most weakly-damped buses susceptible to instability. Specifically, the rotor angles and velocities of the three generating units were identified as the weakest states. The associated generator states indicate the presence of both local and inter-area oscillation modes in the system. Thus, the investigation will incrementally analyze the 3 cases at wind penetration levels of 0.2 p.u., 0.4 p.u., and 0.6 p.u. to assess system stability and oscillatory response. The following sections detail the results at each penetration level:

1- 0.2 p.u.

The system was determined to be stable, as evidenced by all eigenvalues residing in the left half of the complex plane. However, as depicted in Figure 10a, Case 1 appeared the most susceptible to potential instability, with eigenvalues positioned closest to the imaginary axis. In contrast, Cases 2 and 3, as shown in Figures 10b and 10c, demonstrated more robust stability margins, with all eigenvalues farther into the left half-plane (no positive eigenvalues were present). Hence, Final observations from 0.2 p.u. wind penetration:

Case 1 exhibited multiple modes, including both local generator oscillations and an inter-area oscillation:

- A local mode of Generator 3 at 2.0402 Hz (modes 5-6) with 5.2% damping.

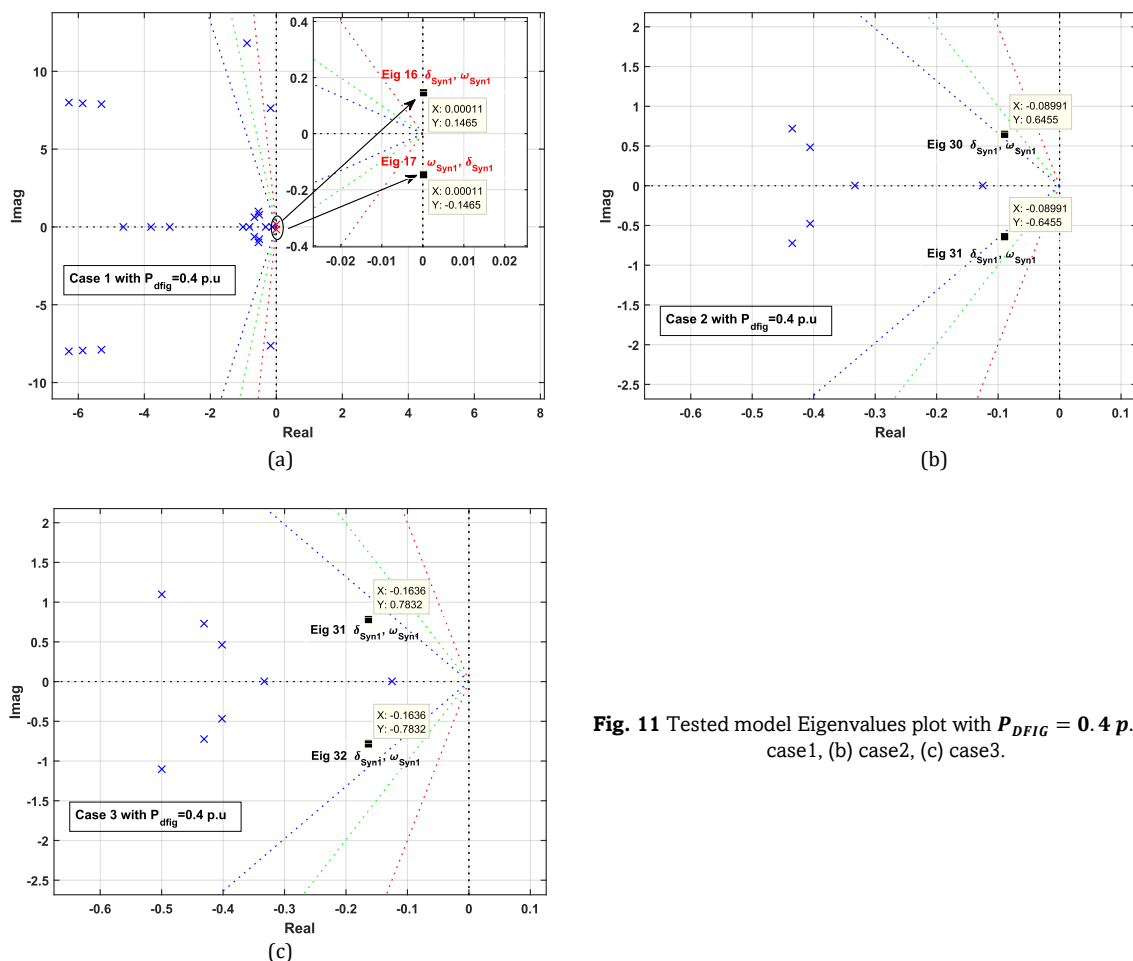


Fig. 11 Tested model Eigenvalues plot with  $P_{DFIG} = 0.4$  p.u (a) case1, (b) case2, (c) case3.

- An inter-area mode between Generators 1 & 2 at 1.3204 Hz (modes 7-8) with very light damping ratio of 1.7%.
- A local under-damped mode of Generator 1 at 0.1339 Hz (modes 19-20).

Cases 2 and 3 only showed localized oscillation modes of Generator 1:

- Case 2 had a Generator 1 local mode at 0.10387 Hz (modes 30-31) with 13.94% damping.
- Case 3 had a Generator 1 local mode at 0.11029 Hz (modes 31-32) with damping of 19.9%.

In summary, Case 1 displayed multiple modes with lighter damping, including risky inter-area oscillations. Cases 2 and 3 had better damped local generator modes indicating more stable operation.

2- 0.4 p.u.

Figure 11a and Table 5 reveal that when the wind power integration level increased to 0.4 p.u., case 1 became marginally unstable because of the emergence of 2 positive eigenvalue in states  $n^{\circ}16/17$  (i.e.,  $(\delta_{Syn1}, \omega_{Syn1})$  and  $(\omega_{Syn1}, \delta_{Syn1})$  with a very low real part of  $+1.1e-4$ ). With the application of PSS and STATCOM, as portrayed in Figures 11b and 11c, the damping of oscillatory modes was increased, restoring stability margins and stabilizing the system. Furthermore, we conclude:

a-For Case 1 at 0.4 p.u.

Case 1 at 0.4 p.u. loading exhibits multiple concerning oscillatory modes: The eigenvalues investigation pointed

several suboptimal system dynamics needing further review. A 1.8818 Hz under-damped local mode of Generator 3 was found, having only 7.5% damping. Also identified was a concerning 1.2116 Hz inter-area mode between Generators 1 & 2 with marginal damping of 2.4%. Most significantly, modes 16-17 exhibited sustained 0.02332 Hz oscillations with zero damping and a slightly positive real part of  $+1.1e-04$ . This corresponds to very low frequency oscillations at 0.02332 Hz, or a 42.84 second period. The problematic oscillations involve states  $\delta_{Syn1}$  and  $\omega_{Syn1}$  of Generator 1. While these oscillations are extremely lightly damped, the system remains practically stable over reasonable timeframes. However, such sustained oscillations are atypical and suggest potential modeling or control issues that should be investigated further. In summary, while still stable, this investigation indicated multiple suboptimal system modes and oscillatory dynamics that warrant deeper review and mitigation efforts.

b-For Cases 2 and 3 at 0.4 p.u.

Local generator modes were observed, reasonably damped in Case 2 at 13.93% and well-damped in Case 3 at 20.88%. To recap, Targeted implementation of supplemental damping controllers enabled stable operation of Case 1 at increased 0.4 p.u. wind integration, despite marginally unstable oscillatory modes, by eliminating positive eigenvalues and restoring stability margins.

3- 0.6 p.u.

Finally, the eigenvalue plots for  $P_{DFIG}=0.6$  p.u. are shown in Figure 12. Similarly to case 1 with 0.4 p.u., 2 positive

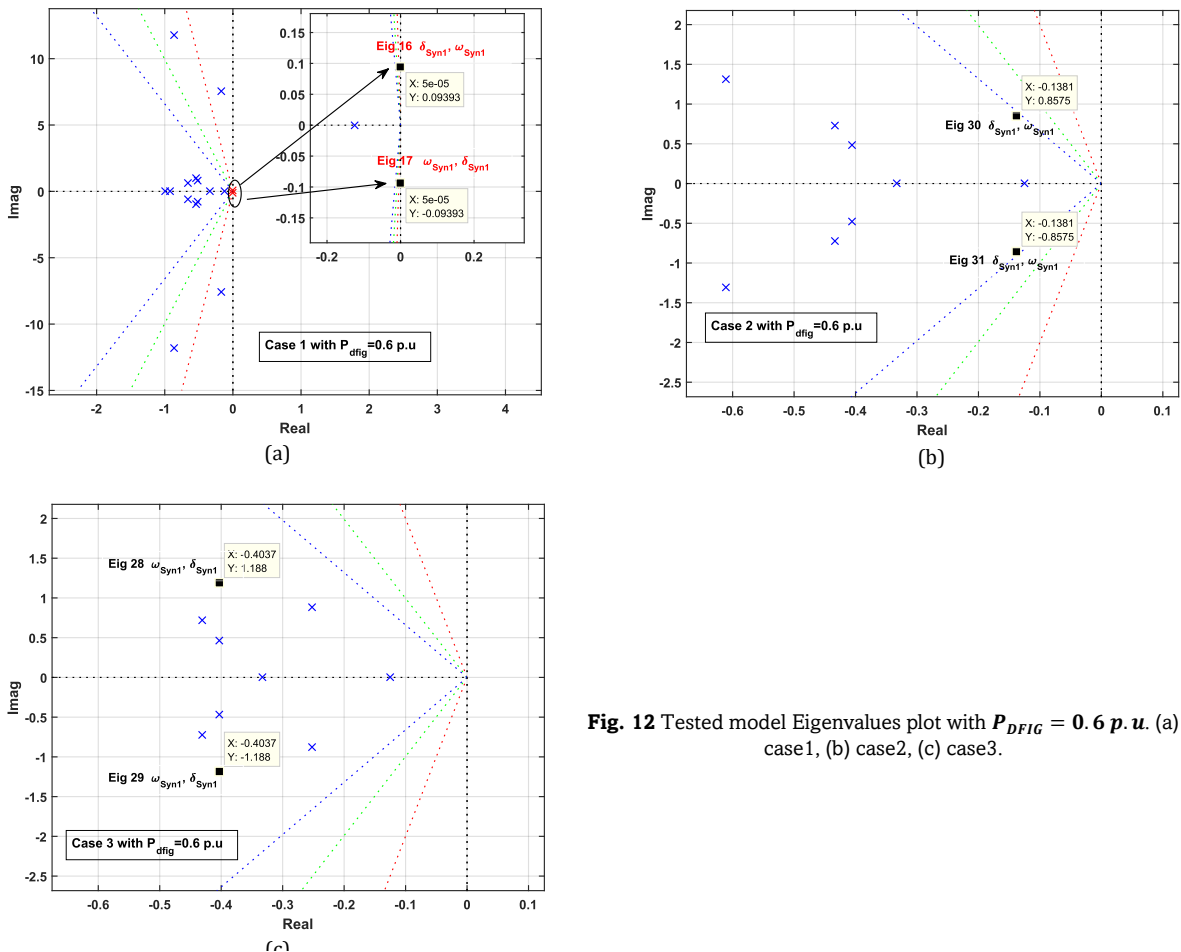


Fig. 12 Tested model Eigenvalues plot with  $P_{DFIG} = 0.6$  p.u. (a) case1, (b) case2, (c) case3.

eigenvalues emerge, causing instability in the slack bus synchronous generator, as seen in Fig 12a. States n°16 ( $\delta_{\text{Syn}_1}$ ,  $\omega_{\text{Syn}_1}$ ) and n°17 ( $\omega_{\text{Syn}_1}$ ,  $\delta_{\text{Syn}_1}$ ) with extremely small positive real parts of  $5e-5$  and imaginary parts of  $\pm 0.09393j$ , as revealed in Table 5, are the primary causes of this marginal instability. In spite of this, plots 12b and 12c demonstrate how the system remains stable despite significant wind penetration, thanks to the controllers' effects. Key findings from the analysis at 0.6 p.u. wind penetration include:

#### a-For Case 1 at 0.6 p.u.

Case 1 at 0.6 p.u. wind integration displays multiple problematic oscillatory modes: The modal analysis revealed several concerning dynamics that warrant further investigation. A risky 1.8807 Hz under-damped local mode of Generator 3 was identified, with only 7.35% damping. Additionally, a hazardous 1.2052 Hz inter-area mode between Generators 1 & 2 exhibited marginal damping of just 2.3%. Most critically, modes 16-17 showed sustained 0.01495 Hz oscillations with near-zero damping and a slightly positive real part of  $+5e-05$ . This points to extremely low frequency oscillations at 0.01495 Hz, corresponding to a 66.8 second period. These problematic oscillations involve states  $\delta_{\text{Syn}_1}$  and  $\omega_{\text{Syn}_1}$  of Generator 1. While technically stable from a positive real part, such dynamics are practically unstable and indicate potential modeling or control issues that should be looked into. Overall, this analysis surfaced multiple areas of the system displaying unfavorable dynamics and oscillations that require mitigation.

#### b-For Cases 2 and 3 at 0.6 p.u.

Cases 2 and 3 maintain adequately damped local generator modes. In a nutshell, at 0.6 p.u. wind power, Case 1 displayed persistent, lightly-damped local and inter-area oscillations, requiring damping control. Case 1 showed a 7.35% damped Generator 3 local mode and concerning 2.3% damped inter-area mode. In contrast, Cases 2 and 3 maintained stability using coordinated PSS-STATCOM damping, achieving 34% damped oscillations in Case 3. This demonstrates the value of complementary damping control to enable higher renewable integration through targeted oscillation mitigation.

## 5. Conclusion

This study analyzes the dynamic response and transient stability of a modified WSCC 9-bus system integrated with a DFIG wind farm under different control configurations. The results demonstrate that a coordinated PSS and STATCOM control strategy provides the best damping performance and stability for the system.

Three operating scenarios were simulated, including no supplementary controls, PSS control only, and combined PSS+STATCOM control. The eigenvalue analysis reveals that as wind penetration increases, the system may exceed safe operating limits without proper controls, leading to instability. The PSS+STATCOM configuration offers significantly improved damping ratios and time-domain responses compared to the other cases.

While the complexity of the power system model constrained the extent of this study, the findings highlight the importance of robust control strategies to maintain stability with high wind power integration. In particular, coordinated PSS and

STATCOM controls are shown to be effective in damping oscillations and transient responses caused by disturbances. Future research should focus on analyzing the impacts of increased renewable penetration on large, complex power grids. Detailed small-signal stability and transient stability studies can identify critical oscillation modes and limit operating conditions to prevent instability. Further work is also needed to develop practical and optimized implementable control solutions that ensure robust system performance under various contingencies and dynamic events.

In summary, this study demonstrates the benefit of a coordinated PSS and STATCOM control strategy for stability enhancement in power systems with high wind penetration. The findings provide an initial platform for further research into implementing robust controls for future renewable-dominant grids.

## Acknowledgments

I would like to acknowledge anyone who helped with this paper

**Author Contributions:** Khaled Kouider: Conceptualization (lead); Methodology (lead); Validation (equal); Writing – original draft (lead); Writing – review & editing (equal). Abdelkader Bekri: Supervision (lead); Validation (equal); Writing – review & editing (equal).

**Funding:** The author(s) received no financial support for the research, authorship, and/or publication of this article.

**Conflicts of Interest:** The authors declare no conflict of interest.

## References

- Adebayo, I. G., & Sun, Y. (2017). New performance indices for voltage stability analysis in a power system. *Energies*, 10(12). <https://doi.org/10.3390/en10122042>
- Agarala, A., Bhat, S. S., Mitra, A., Zychma, D., & Sowa, P. (2022). Transient stability analysis of a multi-machine power system integrated with renewables. *Energies*, 15(13). <https://doi.org/10.3390/en15134824>
- Alsakati, A. A., Vaithilingam, C. A., Alnasseir, J., & Jagadeeshwaran, A. (2022). Simplex Search Method Driven Design for Transient Stability Enhancement in Wind Energy Integrated Power System Using Multi-Band PSS4C. *IEEE Access*, 14, 83913–83928. <https://doi.org/10.1109/ACCESS.2021.3085976>
- Asija, D., Choudekar, P., Soni, K. M., & Sinha, S. K. (2015). Power flow study and contingency status of WSCC 9 Bus test system using MATLAB. <https://dx.doi.org/10.1109/RDCAPE.2015.7281420>
- Avdakovic, S., Nuhanovic, A., Kusljagic, M., Becirovic, E., & Music, M. (2009). Identification of low frequency oscillations in power system. 2009 International Conference on Electrical and Electronics Engineering - ELECO 2009. <https://doi.org/10.1109/ELECO.2009.5355325>
- Bagchi, S., Goswami, S., Bhaduri, R., Ganguly, M., & Roy, A. (2016). Small signal stability analysis and comparison with DFIG incorporated system using FACTS devices. 2016 IEEE 1st International Conference on Power Electronics, Intelligent Control and Energy Systems (ICPEICES) <https://dx.doi.org/10.1109/ICPEICES.2016.7853294>
- Balasubramanian, R., & Singh, R. (2011). Power system voltage stability analysis using ANN and continuation power flow methods. 2011 16th International Conference on Intelligent System Applications to Power Systems, 1–7. <https://dx.doi.org/10.1109/ISAP.2011.6082192>
- Cai, E., Dong, L., & Liao, X. (2021). A reduced-order model for representing the reactive power response of a doubly fed wind turbine during ZVRT. *Journal of Renewable and Sustainable Energy*, 13(5), 053310. <https://doi.org/10.1063/5.0056451>

- Carson W. Taylor, Neal J. Balu, Dominic Maratukulam. (1994). Power system voltage stability. McGraw-Hill, New York.
- Chandra, D. R., Kumari, M. S., Sydulu, M., Grimaccia, F., Mussetta, M., Leva, S., Duong, M.Q. (2014). Impact of SCIG, DFIG wind power plant on IEEE 14 bus system with small signal stability assessment. 2014 Eighteenth National Power Systems Conference (NPSC) <https://dx.doi.org/10.1109/NPSC.2014.7103883>
- Denholm, Paul, Trieu Mai, Rick Wallace Kenyon, Ben Kroposki, and Mark O'Malley. (2020). Inertia and the Power Grid: A Guide Without the Spin (NREL/TP-6120-73856). National Renewable Energy Laboratory (NREL).
- Edrah, M., Lo, K. L., & Anaya-Lara, O. (2015). Impacts of High Penetration of DFIG Wind Turbines on Rotor Angle Stability of Power Systems. *IEEE Transactions on Sustainable Energy*, 6(3), 759–766. <https://doi.org/10.1109/tste.2015.2412176>
- Edrah, M., Lo, K. L., & Anaya-Lara, O. (2016). Reactive power control of DFIG wind turbines for power oscillation damping under a wide range of operating conditions. *IET Generation, Transmission & Distribution*, 10(15), 3777–3785. <https://doi.org/10.1049/iet-gtd.2016.0132>
- Eriksson, R., Modig, N., & Elkington, K. (2018). Synthetic inertia versus fast frequency response: A definition. *IET Renewable Power Generation*, 12(5), 507–514. <https://doi.org/10.1049/iet-rpg.2017.0370>
- Eremia, M., & Shahidepour. (2013). Handbook of Electrical Power System Dynamics: Modeling, Stability, and Control. Wiley.
- Eshkaftaki, A. A., Rabiee, A., Kargar, A., & Boroujeni, S. T. (2020). An Applicable Method to Improve Transient and Dynamic Performance of Power System Equipped With DFIG-Based Wind Turbines. *IEEE Transactions on Power Systems*, 35(3), 2351–2361. <https://doi.org/10.1109/TPWRS.2019.2954497>
- Falehi, A. D., Rostami, M., Doroudi, A., & Ashrafian, A. (2012). Optimization and coordination of SVC-based supplementary controllers and PSSs to improve power system stability using a genetic algorithm. *Turkish Journal of Electrical Engineering and Computer Sciences*, 20(5), 639–654. <https://doi.org/10.3906/elk-1010-838>
- Fdaili, M., Essadki, A., Kharchouf, I., & Nasser, T. (2021). Noncontrolled fault current limiter with reactive power support for transient stability improvement of DFIG-based variable speed wind generator during grid faults. *IET Generation, Transmission & Distribution*, 32(8). <https://doi.org/doi.org/10.1002/2050-7038.12955>
- Gurung, R., N. Bhattacharai, & Kamalasadnan, S. (2020). Optimal Oscillation Damping Controller Design for Large-Scale Wind Integrated Power Grid. *IEEE Transactions on Industry Applications*, 56(4), 4225–4235. <https://doi.org/10.1109/TIA.2020.2988432>
- Hatzigiorgiou, N., Milanovic, J., Rahmann, C., Ajarapu, V., Canizares, C., Erlich, I., Hill, D., Hiskens, I., Kamwa, I., Pal, B., Pourbeik, P., Sanchez-Gasca, J., Stankovic, A., Van Cutsem, T., Vittal, V., & Vournas, C. (2021). Definition and classification of power system stability – revisited & extended. *IEEE Transactions on Power Systems*, 36(4), 3271–3281. <https://doi.org/10.1109/TPWRS.2020.3041774>
- He, P., Fang, Q., Jin, H., Ji, Y., Gong, Z., & Dong, J. (2022). Coordinated design of PSS and STATCOM-POD based on the GA-PSO algorithm to improve the stability of wind-PV-thermal-bundled power system. *International Journal of Electrical Power & Energy Systems*, 141, 108208. <https://doi.org/10.1016/j.ijepes.2022.108208>
- Hemeida, M. G., Rezk, H., & Hamada, M. M. (2018). A comprehensive comparison of STATCOM versus SVC-based fuzzy controller for stability improvement of wind farm connected to multi-machine power system. *Electrical Engineering*, 100(2), 935–951. <https://doi.org/10.1007/s00202-017-0559-6>
- Klein, M., Rogers, G. J., & Prabha, K. (1991). A fundamental study of inter-area oscillations in power systems. *IEEE Transactions on Power Systems*, 6(3), 914–921. <https://doi.org/10.1109/59.119229>
- Kothari, I. J., D. P. Nagrath. (2019). Power System Engineering, 3e. McGraw-Hill Education Pvt. Ltd.
- Kumar, S., Kumar, A., & Sharma, N. K. (2020). A novel method to investigate voltage stability of IEEE-14 bus wind integrated system using PSAT. *Frontiers in Energy*, 14(2), 410–418. <https://doi.org/10.1007/s11708-016-0440-8>
- Li, S., Zhang, H., Yan, Y., & Ren, J. (2022). Parameter Optimization to Power Oscillation Damper (POD) Considering its Impact on the DFIG. *Frontiers in Energy*, 37(2), 1508–1518. <https://doi.org/10.1109/TPWRS.2021.3104816>
- Liu, Y., Liu, Q., Hu, F., Xu, Y., Chen, X., & Chen, S. (2021). Transient stability assessment for power system with wind farm considering the stochasticity. *International Transactions on Electrical Energy Systems*, 14(2). <https://doi.org/10.1002/2050-7038.12854>
- Ma, Y., Lv, S., Zhou, X., & Gao, Z. (2017). Review analysis of voltage stability in power system. 2017 IEEE International Conference on Mechatronics and Automation (ICMA), 7–12. <https://dx.doi.org/10.1109/ICMA.2017.8015779>
- Milano, F. (2008). Power System Analysis Toolbox Version 2.0.0. University College Dublin.
- Miller, T. J. E. (2010). Theory of the doubly-fed induction machine in the steady state. The XIX International Conference on Electrical Machines - ICEM 2010, 1–6. <https://doi.org/10.1109/ICELMACH.2010.5607742>
- Morshed, M. J. (2020). A nonlinear coordinated approach to enhance the transient stability of wind energy-based power systems. *IEEE/CAA Journal of Automatica Sinica*, 7(4), 1087–1097. <https://doi.org/10.1109/JAS.2020.1003255>
- Morshed, M. J., & Fekih, A. (2019). A Probabilistic Robust Coordinated Approach to Stabilize Power Oscillations in DFIG-Based Power Systems. *IEEE Transactions on Industrial Informatics*, 15(10), 5599–5612. <https://doi.org/10.1109/TII.2019.2901935>
- Muñoz, J. C., & Cañizares, C. A. (2011). Comparative stability analysis of DFIG-based wind farms and conventional synchronous generators. 2011 IEEE/PES Power Systems Conference and Exposition. <https://doi.org/10.1109/PSCE.2011.5772545>
- Nkosi, N. R., Bansal, R. C., Adefarati, T., Naidoo, R. M., & Bansal, S. K. (2023). A review of small-signal stability analysis of DFIG-based wind power system. *International Journal of Modelling and Simulation*, 43(3), 153–170. <https://doi.org/10.1080/02286203.2022.2056951>
- Pérez-Londoño, S., Rodríguez-García, L., & López, Y. U. (2012). Effects of doubly fed wind generators on voltage stability of power systems. 2012 Sixth IEEE/PES Transmission and Distribution: Latin America Conference and Exposition (T&D-LA).
- Pillai, A. G., Thomas, P. C., Sreerenjini, K., Baby, S., Joseph, T., & Sreedharan, S. (2013). Transient stability analysis of wind integrate power systems with storage using central area controller. 2013 International Conference on Microelectronics, Communications and Renewable Energy (ICMICR-2013).
- Prabha, K. (1994). *Power System Stability and Control*. McGraw-Hill Education, New York.
- Qiao, W., Venayagamoorthy, G. K., & Harley, R. G. (2009). Real-time implementation of a STATCOM on a wind farm equipped with doubly fed induction generators. *IEEE Transactions on Industry Applications*, 45(1), 98–107. <https://doi.org/10.1109/TIA.2008.2009377>
- Ramanujam, R. (2010). Power System Dynamics: Analysis and Simulation. PHI Learning Pvt. Ltd.
- Reza, M., Sloopweg, J. G., Schavemaker, P. H., Kling, W. L., & van der Sluis, L. (2003). Investigating impacts of distributed generation on transmission system stability. 2003 IEEE Bologna Power Tech Conference Proceedings, 2, 7 pp. Vol.2-. <https://doi.org/10.1109/PTC.2003.1304341>
- Shabani, H. R., & Kalantar, M. (2021). Real-time transient stability detection in the power system with high penetration of DFIG-based wind farms using transient energy function. *International Journal of Electrical Power & Energy Systems*, 131. <https://doi.org/10.1016/j.ijepes.2021.107319>
- Shabani, H. R., Kalantar, M., & Hajizadeh, A. (2021). Investigation of the closed-loop control system on the DFIG dynamic models in transient stability studies. *International Journal of Electrical Power & Energy Systems*, 131. <https://doi.org/10.1016/j.ijepes.2021.107084>
- Shahgholian, G., & Izadpanahi, N. (2016). Improving the performance of wind turbine equipped with DFIG using STATCOM based on input-output feedback linearization controller. *Environmental Engineering Science*, 4, 65–79.

- [https://www.energyequipsys.com/article\\_20128\\_8c989427ad8dfacc589a02518a7e584f.pdf](https://www.energyequipsys.com/article_20128_8c989427ad8dfacc589a02518a7e584f.pdf)
- Simani, S., & Farsoni, S. (2018). Introduction. In Farsoni, S. Simani, S. (Ed.), *Fault Diagnosis and Sustainable Control of Wind Turbines* (pp. 1–12). Butterworth-Heinemann, Elsevier.
- Simon, L., Ravishankar, J., & Swarup, K. S. (2019). Coordinated reactive power and crow bar control for DFIG-based wind turbines for power oscillation damping. *Wind Engineering*, 43(2), 95–113. <https://doi.org/10.1177/0309524X18780385>
- Tang, W., Hu, J., Chang, Y., & Liu, F. (2018). Modeling of DFIG-Based wind turbine for power system transient response analysis in rotor speed control timescale. *IEEE Transactions on Power Systems*, 33(6), 6795–6805. <https://doi.org/10.1109/TPWRS.2018.2827402>
- THANPISIT, K., & NGAMROO, I. (2017). Power oscillation damping control by PSS and DFIG wind turbine under multiple operating conditions. *Turkish Journal of Electrical Engineering and Computer Sciences*, 25(5), 4354–4368. <https://doi.org/10.3906/elk-1702-190>
- Xia, S., Zhang, Q., Hussain, S. T., Hong, B., & Zou, W. (2018). Impacts of integration of wind farms on power system transient stability. *Applied Sciences*, 8(8). <https://doi.org/10.3390/app8081289>
- Xu, Y., Chi, Y., & Yuan, H. (2023). Power system stability. In *Stability-constrained optimization for modern power system operation and planning* (pp. 5–18). <https://doi.org/10.1002/9781119848899.ch1>
- Yang, B., Jiang, L., Wang, L., Yao, W., & Wu, Q. H. (2016). Nonlinear maximum power point tracking control and modal analysis of DFIG based wind turbine. *International Journal of Electrical Power & Energy Systems*, 74, 429–436. <https://doi.org/10.1016/j.ijepes.2015.07.036>
- Yang, L., Xu, Z., Østergaard, J., Dong, Z. Y., Wong, K. P., & X. Ma. (2011). Oscillatory Stability and Eigenvalue Sensitivity Analysis of A DFIG Wind Turbine System. *IEEE Transactions on Energy Conversion*, 26(1), 328–339. <https://doi.org/10.1109/TEC.2010.2091130>
- Yu, S. S., Chau, T. K., Fernando, T., & Iu, H. H. (2018). An Enhanced Adaptive Phasor Power Oscillation Damping Approach With Latency Compensation for Modern Power Systems. *IEEE Transactions on Power Systems*, 33(4), 4285–4296. <https://doi.org/10.1109/TPWRS.2017.2773632>
- Yunus, A. M. S., Saini, M., Djalal, M. R., Abu-Siada, A., & Masoum, M. A. S. (2019). Impact of superconducting magnetic energy storage unit on doubly fed induction generator performance during various levels of grid faults. *International Review of Electrical Engineering (IREE)*, 14. <https://doi.org/10.15866/iree.v14i4.16472>
- Zhang, C., Ke, D., Sun, Y., Chung, C. Y., Xu, J., & Shen, F. (2018). Coordinated Supplementary Damping Control of DFIG and PSS to Suppress Inter-Area Oscillations with Optimally Controlled Plant Dynamics. *IEEE Transactions on Sustainable Energy*, 9(2), 780–791. <https://doi.org/10.1109/TSTE.2017.2761813>
- Zheng, D., Jinxin, O., Xiaofu, X., & Mengyang, L. (2019). Rotor angle stability control for DFIG-integrated power system considering phase-amplitude characteristics of transient-grid voltage. *IET Generation, Transmission & Distribution*, 13(16), 3549–3555. <https://doi.org/10.1049/iet-gtd.2018.6960>



© 2023. The Author(s). This article is an open access article distributed under the terms and conditions of the Creative Commons Attribution-ShareAlike 4.0 (CC BY-SA) International License (<http://creativecommons.org/licenses/by-sa/4.0/>)